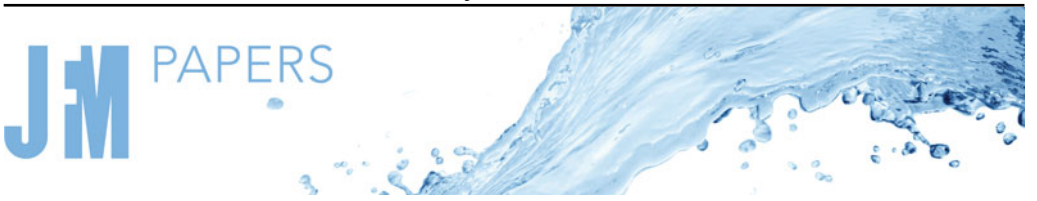
J. Fluid Mech. (2026), *vol.* 1030, A47, doi:10.1017/jfm.2026.11276



Membrane heterogeneity-driven dynamics of multicomponent vesicles in shear flow

Shuqi Tang[1], **Steven M. Wise**[2], **John S. Lowengrub**[3] **and Zhenlin Guo**[1]

[1]Beijing Computational Science Research Center, Beijing 100193, PR China

[2]Department of Mathematics, The University of Tennessee, Knoxville, TN 37996, USA

[3]Department of Mathematics, University of California Irvine, Irvine, CA 92697, USA

Corresponding author: Zhenlin Guo, zguo@csrc.ac.cn

(Received 10 September 2025; revised 5 December 2025; accepted 31 January 2026)

Despite its significance in biology and materials science, the dynamics of multicomponent vesicles under shear flow remains poorly understood because of its nonlinear and strongly coupled nature, especially regarding the role of membrane heterogeneity in driving non-equilibrium behaviour. Here we present a thermodynamically consistent phase-field model, which is validated against experiments, for the quantitative investigation of the dynamics. While prior research has primarily focused on viscosity or bending rigidity contrasts, we demonstrate that surface tension heterogeneity can also trigger swinging and tumbling in vesicles under shear. Additionally, our systematic phase diagram reveals three previously unreported dynamical regimes arising from the interplay between bending rigidity heterogeneity and shear flow. Overall, our model provides a robust framework for understanding multicomponent vesicle dynamics, with findings offering new physical insights and design principles for tuneable vesicle-based carriers.

Key words: membranes, multiphase flow

1. Introduction

Multicomponent lipid vesicles – composed of saturated lipids, unsaturated lipids and cholesterol – serve as minimal models for biological membranes. Their lateral phase separation into liquid-ordered (l_o) and liquid-disordered (l_d) domains (Baumgart, Hess & Webb 2003; Veatch & Keller 2003, 2005; Lingwood & Simons 2010; Wang *et al.* 2022) leads to spatial heterogeneity in membrane properties such as bending rigidity and surface tension (Evans & Rawicz 1990; Baumgart *et al.* 2005; Yanagisawa, Imai & Taniguchi 2008). These heterogeneities underlie lipid rafts, which play critical roles in signal transduction (Simons & Ikonen 1997; Simons & Toomre 2000; Sackmann & Smith 2014), membrane trafficking (Simons & Vaz 2004) and molecular sorting (Mukherjee &

© The Author(s), 2026. Published by Cambridge University Press.

https://doi.org/10.1017/jfm.2026.11276 Published online by Cambridge University Press

Maxfield 2004). Understanding how such heterogeneity modulates membrane deformation under flow is crucial for the design of biomimetic materials (Elani, Law & Ces 2014) and drug delivery in cell biology (Allen & Cullis 2004; Herrmann, Wood & Fuhrmann 2021; Kooijmans *et al.* 2021; Karaz & Senses 2023).

The dynamics of single-component vesicles in shear flow has been extensively investigated through experimental, theoretical and numerical methods, revealing a rich variety of behaviours such as tank treading, tumbling and swinging, primarily driven by viscosity contrast (Keller & Skalak 1982; Abkarian & Viallat 2005; Kantsler & Steinberg 2006; Misbah 2006; Danker *et al.* 2007; Noguchi & Gompper 2007; Vlahovska & Gracia 2007; Lebedev, Turitsyn & Vergeles 2008; Deschamps, Kantsler & Steinberg 2009). In contrast, the dynamics of multicomponent vesicles under shear flow remains poorly understood. Two-dimensional simulations have successfully reproduced phase treading and tumbling driven by bending heterogeneity and asymmetric phase distributions (Lowengrub, Xu & Voigt 2007; Sohn *et al.* 2010; Liu *et al.* 2017; Gera, Salac & Spagnolie 2022). However, these models are limited to planar dynamics and cannot account for three-dimensional (3-D) phenomena, such as vertical ring banding (Gera & Salac 2018*a*,*b*), neither can they incorporate line tension, which experimental studies have shown can induce tumbling (Tusch *et al.* 2018). Recent 3-D simulations provide insights into the interplay of bending heterogeneity and flow (Venkatesh & Narsimhan 2024), but are limited by assumptions of small deformations and neglect surface tension heterogeneity. Likewise, the two-phase fluid deformable surface sharp-interface model proposed in Sischka & Voigt (2025) incorporates bending heterogeneity but fails to capture topological transitions accounting for surface tension heterogeneity. To our knowledge, most numerical models enforce local membrane inextensibility by introducing a spatially varying Lagrange multiplier Arroyo & DeSimone (2009), Veerapaneni *et al.* (2011), Sohn *et al.* (2012), Aland *et al.* (2014), Young, Veerapaneni & Miksis (2014), Lowengrub, Allard & Aland (2016), often interpreted as an surface tension – a purely kinematic reaction field. Although composition-dependent tensions appear in several theoretical frameworks Lowengrub *et al.* (2007), Li, Lowengrub & Voigt (2012), Destainville, Manghi & Cornet (2018), Wu & Ou-Yang (2025), the dynamical consequences of the associated thermodynamic tension gradients have received relatively little attention.

To overcome these limitations, we developed a thermodynamically consistent phase-field model for multicomponent vesicles under shear flow. Our model effectively captures the coupling between background fluid and membrane dynamics, together with lateral phase separation, while incorporating line tension and component-dependent physical properties. Our 3-D simulations demonstrate excellent qualitative and quantitative agreement with experimental observations, accurately capturing phase separation and shear-induced dynamics. We further explore how shear-induced dynamics are governed by bending rigidity heterogeneity ($\kappa_B = \kappa_{B_{l_d}}/\kappa_{B_{l_o}}$), surface tension heterogeneity ($\sigma_S = \sigma_{S_{l_d}}/\sigma_{S_{l_o}}$) and bending capillary number $Ca = \mu_{out} U L^2/\kappa_{B_{l_o}}$. Our results uncover a range of complex dynamic regimes, including three previously unreported ones. Notably, we identify a surface-tension-driven swinging and tumbling mechanism that arises without viscosity contrast or asymmetric phase distributions. These findings reveal previously unexplored physical pathways for regulating vesicle dynamics and offer guidance for biomimetic vesicle design in flow environments.

The outline of the paper is as follows. Section 2 presents a thermodynamically consistent phase-field model for multicomponent vesicles, and introduces key dimensionless parameters. Section 3 validates the model against experimental observations (Tusch *et al.* 2018; Wang *et al.* 2022). Section 4 reports numerical results, elucidating the interplay

https://doi.org/10.1017/jfm.2026.11276 Published online by Cambridge University Press

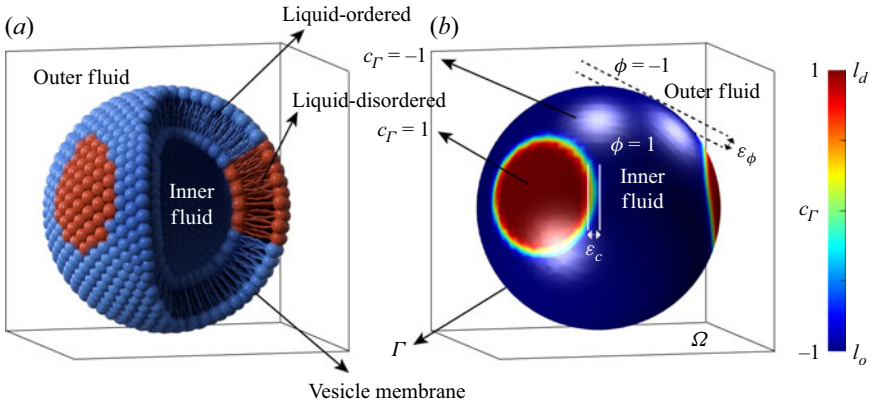


Figure 1. (*a*) A multicomponent vesicle with lipid components (l_d (red) and l_o (blue)) exhibiting distinct properties, immersed in a background fluid, illustrating the lipid bilayer structure. For simplicity, the two components are distinguished only by colour. (*b*) Diffuse-interface representation of panel (*a*), showing the corresponding phase-field distribution.

between membrane heterogeneity and flow-induced forces. The appendices present additional methodological and numerical details.

2. Model

In this section, we develop a thermodynamically consistent phase-field model derived from the total energy of the system to investigate the dynamics of multicomponent vesicles with membrane heterogeneity under shear flow within a rectangular domain Ω (see figure 1).

2.1. *Governing equations for vesicle membrane interacting with background fluid*

We consider a vesicle immersed in a background fluid within a rectangular domain Ω, whose membrane is represented by a closed surface Γ. The system is modelled as a two-phase flow, with Γ serving as the interface between the inner and outer fluids. To capture complex shape deformations, we adopt a phase-field formulation in which the sharp interface Γ is replaced by a diffuse interface characterized by a scalar field $\phi(\boldsymbol{x}, t)$. The phase-field variable ϕ follows a hyperbolic tangent profile across the membrane interface, ensuring a smooth transition from the interior ($\phi = 1$) to the exterior ($\phi = -1$) of the vesicle. Specifically, ϕ can be defined as

$$\phi(\boldsymbol{x}, t) = \tanh\left(\frac{r(\boldsymbol{x}, t)}{2\sqrt{2}\varepsilon_\phi}\right), \quad \boldsymbol{x} \in \bar{\Omega}, \tag{2.1}$$

where $r(\boldsymbol{x}, t)$ denotes the signed distance from $\boldsymbol{x}$ to the nearest point on the membrane interface Γ, taken positive inside and negative outside, and ε_ϕ controls the thickness of the diffuse interface.

Both the inner and outer fluids are assumed to be incompressible, with equal density ($\rho_{in} = \rho_{out}$) but distinct viscosities, denoted by μ_{in} and μ_{out}. The governing equations for the coupled two-phase flow and membrane evolution are formulated as follows:

$$(\rho\boldsymbol{u})_t + \nabla\cdot(\rho\boldsymbol{u}\otimes\boldsymbol{u}) = \nabla\cdot(\mu\boldsymbol{D}(\boldsymbol{u})) - \nabla p + \boldsymbol{F} + \nabla\cdot(\zeta(\phi)\boldsymbol{P}\lambda_{local}), \tag{2.2}$$

$$\nabla\cdot\boldsymbol{u} = 0, \tag{2.3}$$

https://doi.org/10.1017/jfm.2026.11276 Published online by Cambridge University Press

$$\phi_t + \nabla \cdot (\phi \boldsymbol{u}) = \nabla \cdot \boldsymbol{q}_{\boldsymbol{\phi}}, \tag{2.4}$$

$$\xi \varepsilon_\phi^2 \nabla \cdot (\phi^2 \nabla \lambda_{local}) + \zeta(\phi) \boldsymbol{P} : \nabla \boldsymbol{u} = 0, \tag{2.5}$$

where (2.2) and (2.3) represent the conservation of momentum and fluid incompressibility via the Navier–Stokes equations, and (2.4) describes the evolution of the vesicle membrane using a phase-field Cahn–Hilliard (CH) formulation. The membrane inextensibility condition is enforced through (2.5). Here, $\boldsymbol{u}$ and p denote the bulk velocity and pressure, respectively. The rate of strain tensor is given by $\boldsymbol{D}(\boldsymbol{u}) = (\nabla \boldsymbol{u} + \nabla \boldsymbol{u}^T)/2$. The spatially varying viscosity is interpolated as $\mu(\phi) = (1-\phi)\mu_{in}/2 + (1+\phi)\mu_{out}/2$. The vesicle–fluid interaction force $\boldsymbol{F}$ and the interfacial flux $\boldsymbol{q}_\phi$ will be defined later.

In addition, membrane inextensibility is modelled using the diffuse domain approach of Aland *et al.* (2014), which extends the local surface constraint $\nabla_\Gamma \cdot \boldsymbol{u} = \boldsymbol{P} : \nabla \boldsymbol{u} = 0$ from the vesicle membrane Γ to the entire computational domain Ω. Here, the surface gradient operator is defined as

$$\nabla_\Gamma = \boldsymbol{P} \nabla = \nabla - \boldsymbol{n}(\boldsymbol{n} \cdot \nabla), \tag{2.6}$$

where $\boldsymbol{P} = \boldsymbol{I} - \boldsymbol{n} \otimes \boldsymbol{n}$ denotes the projection tensor onto the tangential plane of the membrane, with the unit normal vector $\boldsymbol{n} = -\nabla\phi/|\nabla\phi|$ pointing from the interior to the exterior of the vesicle. The inextensibility constraint is enforced by introducing a local Lagrange multiplier λ_{local} together with a harmonic regularization term, leading to (2.5), where the parameter $\xi > 0$ controls the strength of the regularization. The regularized surface delta function is then defined as

$$\zeta(\phi) = \eta_\phi \left(\frac{f(\phi)}{\varepsilon_\phi} + \frac{\varepsilon_\phi}{2} |\nabla \phi|^2 \right), \tag{2.7}$$

where $f(\phi) = (1-\phi^2)^2/4$ is a double-well potential, ε_ϕ is the membrane thickness and η_ϕ is a scaling parameter that relates the diffuse interface to the sharp-interface model. The resulting constraint term contributes additional membrane tension forces in the momentum equation, completing the formulation of (2.2).

Furthermore, the velocity $\boldsymbol{u}$ is subject to Dirichlet boundary conditions, while the phase-field variable ϕ and its associated flux $\boldsymbol{q}_\phi$ satisfy no-flux boundary conditions,

$$\boldsymbol{u} = \boldsymbol{u}_{\boldsymbol{bc}} \quad \text{on} \quad \partial\Omega, \tag{2.8}$$

$$\boldsymbol{n}_{\boldsymbol{b}} \cdot \nabla \phi = \boldsymbol{n}_{\boldsymbol{b}} \cdot \boldsymbol{q}_{\boldsymbol{\phi}} = 0 \qquad \text{on} \quad \partial\Omega, \tag{2.9}$$

where $\boldsymbol{n}_{\boldsymbol{b}}$ denotes the unit outward normal vector to the boundary $\partial\Omega$ of the rectangular computational domain Ω.

2.2. *Governing equation for multicomponent on the vesicle membrane*

We model the vesicle membrane Γ as a two-phase fluid consisting of liquid-ordered (l_o) and liquid-disordered (l_d) phases with distinct physical properties. The membrane composition is described by a second scalar phase-field variable c_Γ defined on the membrane Γ, where $c_\Gamma = 1$ corresponds to the l_d phase, and $c_\Gamma = -1$ to the l_o phase. The two components are separated by a diffuse interface of thickness ε_c, across which c_Γ transitions smoothly. The phase separation dynamics on Γ are governed by the surface CH equation (Zhiliakov *et al.* 2021),

$$(c_\Gamma)_t + \nabla_{\boldsymbol{\Gamma}} \cdot (c_\Gamma \boldsymbol{u}) = \nabla_{\boldsymbol{\Gamma}} \cdot \boldsymbol{q}_{\boldsymbol{c}}, \tag{2.10}$$

where the diffusive flux of the membrane component, $\boldsymbol{q}_c$, will be specified later.

https://doi.org/10.1017/jfm.2026.11276 Published online by Cambridge University Press

To couple the surface phase dynamics (2.10) with the bulk phase-field system (2.2)–(2.5) in the rectangular domain Ω, we employ the diffuse domain method (Rätz & Voigt 2006; Li *et al.* 2009; Teigen *et al.* 2009), which is an accurate and efficient numerical approach for solving partial differential equations (PDEs) on complex surfaces. The vesicle membrane Γ is embedded into the larger, rectangular domain Ω using a regularized surface delta function $\zeta(\phi)$ derived from the phase-field variable ϕ. This embedding eliminates the need for explicit interface tracking. Moreover, the method establishes a unified, energy-based framework by extending surface PDEs into the bulk domain Ω through the regularized delta function $\zeta(\phi)$ (2.7). Accordingly, the surface CH (2.10) is reformulated in Ω as

$$(\zeta(\phi)c_\Gamma)_t + \nabla\cdot(\zeta(\phi)c_\Gamma \boldsymbol{u}) = \nabla\cdot(\zeta(\phi)\boldsymbol{q_c})\,. \tag{2.11}$$

Details of this extension are provided in Appendix A. Notably, previous studies have demonstrated that in the diffuse domain method, the extended PDE (2.11) asymptotically converges to the original surface PDE (2.10) as the diffuse interface thickness approaches zero ($\varepsilon_\phi \to 0$) (Li *et al.* 2009; Yu, Chen & Thornton 2012; Lervåg & Lowengrub 2015; Chadwick *et al.* 2018; Poulsen & Voorhees 2018; Yu, Guo & Lowengrub 2020; Guo *et al.* 2021; Guo 2023).

In addition, the membrane component c_Γ and its flux $\boldsymbol{q_c}$ are subject to no-flux boundary conditions on the boundary of the rectangular domain Ω,

$$\boldsymbol{n_b}\cdot\nabla \boldsymbol{c_\Gamma} = \boldsymbol{n_b}\cdot\boldsymbol{q_c} = 0 \quad \text{on} \quad \partial\Omega. \tag{2.12}$$

Thanks to the diffuse domain method, the membrane component equation for c_Γ (2.11) can be naturally coupled with the vesicle–fluid interaction system (2.2)–(2.5) and solved simultaneously within the same rectangular domain Ω. The unknown terms $\boldsymbol{F}$, $\boldsymbol{q_\phi}$ and $\boldsymbol{q_c}$ in (2.2)–(2.5) and (2.11) will be derived via an energy-variation approach based on the principle of free energy dissipation, thereby ensuring thermodynamic consistency.

2.3. *Free energy of the multicomponent vesicle–fluid system*

The free energy $\mathcal{F}$ of a multicomponent vesicle immersed in a background fluid comprises contributions from both the fluid and the membrane. These include the kinetic energy of the background fluid $\mathcal{F}_K$, the membrane bending energy $\mathcal{F}_B$, the surface energy $\mathcal{F}_S$, the line energy $\mathcal{F}_L$ and a penalty term $\mathcal{F}_A$ enforcing surface area conservation. The free energy is expressed as

$$\begin{aligned}\mathcal{F} &= \mathcal{F}_K + \mathcal{F}_B + \mathcal{F}_S + \mathcal{F}_L + \mathcal{F}_A \\ &= \int_\Omega \frac{1}{2}\rho|\boldsymbol{u}|^2\,\mathrm{d}V + \int_\Omega \frac{1}{2\varepsilon_\phi}\kappa_B(c_\Gamma)\omega_\phi^2\,\mathrm{d}V + \int_\Omega \sigma_S(c_\Gamma)\zeta(\phi)\,\mathrm{d}V \\ &\quad + \int_\Omega \sigma_L\zeta(c_\Gamma)\zeta(\phi)\,\mathrm{d}V \;+ \frac{M_s}{2}\frac{(S(\phi)-S(\phi_0))^2}{S(\phi_0)}.\end{aligned} \tag{2.13}$$

In the bending energy $\mathcal{F}_B$, the scalar field

$$\omega_\phi = \eta_\phi\left(\frac{f'(\phi)}{\varepsilon_\phi} - \varepsilon_\phi\Delta\phi\right), \tag{2.14}$$

serves as a phase-field approximation of the membrane mean curvature. Here, zero spontaneous curvature is assumed and the contribution from Gaussian curvature is neglected. The bending rigidity $\kappa_B(c_\Gamma)$, associated with the bending energy $\mathcal{F}_B$, and the surface tension $\sigma_S(c_\Gamma)$, defined in the surface energy $\mathcal{F}_S$, are both modelled as functions

https://doi.org/10.1017/jfm.2026.11276 Published online by Cambridge University Press

of the membrane component field c_Γ,

$$\kappa_B(c_\Gamma) = \frac{1+c_\Gamma}{2}\kappa_{B_{l_d}} + \frac{1-c_\Gamma}{2}\kappa_{B_{l_o}}, \quad \sigma_S(c_\Gamma) = \frac{1+c_\Gamma}{2}\sigma_{S_{l_d}} + \frac{1-c_\Gamma}{2}\sigma_{S_{l_o}}. \tag{2.15}$$

In the line energy $\mathcal{F}_L$, the function

$$\zeta(c_\Gamma) = \eta_c\left(\frac{f(c_\Gamma)}{\varepsilon_c} + \frac{\varepsilon_c}{2}|\nabla c_\Gamma|^2\right) \tag{2.16}$$

serves as a regularized delta function that captures the diffuse interface between membrane components. Here, the double-well potential $f(c_\Gamma) = (1-c_\Gamma^2)^2/4$ promotes phase separation, ε_c represents the interfacial thickness between the components, η_c is a scaling parameter and σ_L denotes the line tension. In the penalty energy $\mathcal{F}_A$, the vesicle surface area is defined as $S(\phi) = \int_\Omega \zeta(\phi)\,\mathrm{d}V$. The reference area $S(\phi_0)$ is measured at the initial time $t = 0$ and assumed constant during the simulation. Surface area conservation is enforced by this penalty term, with its strength controlled by the penalty coefficient M_S, which has been found to help improve the accuracy of the method (Aland *et al.* 2014).

By applying an energy-variation approach, we derive explicit expressions for the terms $\boldsymbol{F}$, $\boldsymbol{q_\phi}$ and $\boldsymbol{q_c}$ that were previously left unspecified in the governing equations. Detailed derivations are provided in Appendix B.

2.4. *Non-dimensionalization*

To non-dimensionalize the model, we choose the characteristic length, velocity and time scales as L, U and L/U, respectively. Fluid properties are normalized with respect to the outer fluid (where $\phi = -1$), using characteristic viscosity μ_{out} and density ρ_{out}, while membrane properties are normalized by those of the l_o phase ($c_\Gamma = -1$). The non-dimensional form of the multicomponent vesicles–fluid model is then given by

$$(\rho\boldsymbol{u})_t + \nabla\cdot(\rho\boldsymbol{u}\otimes\boldsymbol{u}) = \frac{1}{Re}\nabla\cdot(\mu\boldsymbol{D}(\boldsymbol{u})) - \nabla p + \frac{1}{Re}\boldsymbol{F} + \nabla\cdot(\zeta(\phi)\boldsymbol{P}\lambda_{local}), \tag{2.17}$$

$$\nabla\cdot\boldsymbol{u} = 0, \tag{2.18}$$

$$\phi_t + \nabla\cdot(\phi\boldsymbol{u}) = \frac{1}{Pe}\nabla\cdot\boldsymbol{q_\phi}, \tag{2.19}$$

$$\xi{\varepsilon_\phi}^2\nabla\cdot\left(\phi^2\nabla\lambda_{local}\right) + \zeta(\phi)\boldsymbol{P}:\nabla\boldsymbol{u} = 0, \tag{2.20}$$

$$(\zeta(\phi)c_\Gamma)_t + \nabla\cdot(\zeta(\phi)c_\Gamma\boldsymbol{u}) = \frac{1}{Pe_\Gamma}\nabla\cdot(\zeta(\phi)\boldsymbol{q_c}), \tag{2.21}$$

where

$$\boldsymbol{F} = g\nabla\phi + \omega_c\nabla(\zeta(\phi)c_\Gamma), \tag{2.22}$$

$$\boldsymbol{q_\phi} = m(\phi)\nabla g, \tag{2.23}$$

$$\boldsymbol{q_c} = m(c_\Gamma)\nabla\omega_c, \tag{2.24}$$

with

$$g = b\omega_\phi + \frac{1}{Ca}\left(\kappa_B(c_\Gamma)\eta_\phi\frac{f''(\phi)}{{\varepsilon_\phi}^2}\omega_\phi - \eta_\phi\Delta(\kappa_B(c_\Gamma)\omega_\phi)\right) - \eta_\phi\varepsilon_\phi\nabla b\cdot\nabla\phi, \tag{2.25}$$

$$b = -\omega_c c_\Gamma + Cn_\Gamma\delta(c_\Gamma) + \mathcal{M}_s\frac{S(\phi)-S(\phi_0)}{S(\phi_0)} + Cs_\Gamma\sigma_S(c_\Gamma). \tag{2.26}$$

https://doi.org/10.1017/jfm.2026.11276 Published online by Cambridge University Press

The chemical potential associated with the membrane component field c_Γ is given by

$$\zeta(\phi)\omega_c = \frac{1}{Ca}\frac{{\varepsilon_\phi}^{-1}}{2}{\kappa_B}'(c_\Gamma){\omega_\phi}^2 + Cs{\sigma_S}'(c_\Gamma)\zeta(\phi) + Cn_\Gamma\zeta(\phi)\left(\eta_c\frac{f'(c_\Gamma)}{\varepsilon_c} - \eta_c\varepsilon_c\Delta c_\Gamma\right) - Cn_\Gamma\eta_c\varepsilon_c\nabla\zeta(\phi)\cdot\nabla c_\Gamma. \quad (2.27)$$

Equations (2.17) and (2.18) describe the dynamics of the incompressible background fluid, while the evolution of the vesicle membrane is governed by (2.19). The local inextensibility of the vesicle is enforced via (2.20), and the lateral phase separation of membrane components is governed by (2.21). The boundary conditions are applied as specified in (2.8), (2.9) and (2.12).

Notably, we emphasize that $\sigma(c_\Gamma)$ and λ_{local} play fundamentally different roles in our model. The field λ_{local} arises solely from the geometric inextensibility constraint and therefore cannot represent composition-dependent surface tension. In contrast, $\sigma(c_\Gamma)$ is a genuine material property that encodes the membrane's intrinsic energetics, and its spatial gradients can actively drive Marangoni-type tangential flows. Thus, the two quantities operate at distinct physical levels: λ_{local} enforces kinematic inextensibility, whereas $\sigma(c_\Gamma)$ governs the membrane's thermodynamic response to compositional heterogeneity. Although their associated tangential stresses may locally reinforce or partially counteract each other under certain flow conditions, the constraint-induced tension cannot generally replace or compensate for material surface tension since it is uniquely determined by the inextensibility requirement. A systematic investigation of how constraint-induced tension redistributes in the presence of heterogeneous material tension is beyond the scope of the present work and will be considered in future studies.

The vesicle dynamics described by (2.17)–(2.27) are governed by a set of dimensionless parameters that characterize the coupling between the background fluid and membrane dynamics, the lateral phase separation and the influence of line tension and component-dependent physical properties. These dimensionless parameters are summarized in table 1.

Our model integrates key physical features, including membrane component-dependent bending rigidity heterogeneity, surface tension heterogeneity, line tension, inextensibility and viscosity contrasts between the internal and external fluids. Its thermodynamically consistent formulation ensures free energy dissipation and physical consistency, enabling the simulation of complex dynamic processes under realistic biological conditions. This comprehensive framework provides a powerful tool for investigating vesicle behaviour under shear flow and for elucidating the role of membrane heterogeneity in governing non-equilibrium dynamics.

3. Numerical validations

To validate the model, we conducted systematic comparisons between our simulations and two sets of experimental observations: (i) phase separation dynamics on giant unilamellar vesicles (GUVs) reported in Wang *et al.* (2022), and (ii) dynamic behaviours of prepositioned multicomponent vesicles under shear flow reported in Tusch *et al.* (2018). The numerical method is detailed in Appendix C, and additional numerical convergence tests are presented in Appendix D to verify the accuracy of the diffuse-interface formulation and to validate both the numerical method and the spatial–temporal resolutions used in all simulations. At the fully discrete level, we employ BSAM – a highly efficient block-structured adaptive full approximation scheme multigrid solver – for the simulations. The solver combines a staggered finite-difference method with a full

https://doi.org/10.1017/jfm.2026.11276 Published online by Cambridge University Press

Symbol	Expression	Description	Typical value
Fluid parameters			
ρ	—	Fluid density (inside and outside equal)	$\rho_{in} = \rho_{out} \approx 1000$ kg m^{-3} Luby-Phelps (1999*a*)
$\mu(\phi)$	$(1+\phi)\mu_{in}/2 + (1-\phi)\mu_{out}/2$	Fluid viscosity	$\mu_{in} \approx 0.001-0.10$ Pa s, $\mu_{out} \approx 0.001-0.01$ Pa s Luby-Phelps (1999*a*), Wirtz (2009)
Diffuse-interface membrane parameters			
ε_ϕ	—	Membrane diffuse interface thickness	≈ 5 nm Regan *et al.* (2019), Risselada & Marrink (2008)
$m(\phi)$	$D_\phi(1-\phi^2)^2$	Mobility of ϕ (controls interfacial relaxation)	$D_\phi \sim 10^{-15}-10^{-13}$ m^3 s^{-1} Luby-Phelps (1999*a*)
M_S	—	Surface-area penalty coefficient	—
ξ	—	Inextensibility relaxation parameter	—
Membrane component parameters			
ε_c	—	Component diffuse interface thickness	—
$m(c_\Gamma)$	$D_c(1-c_\Gamma^2)^2$	Mobility of c_Γ (lateral diffusion)	$D_c \sim 10^{-12} - 10^{-10}$ m^2 s^{-1} Lindblom & Orädd (1994)
$\kappa_B(c_\Gamma)$	$\frac{1+c_\Gamma}{2}\kappa_{B_{l_d}} + \frac{1-c_\Gamma}{2}\kappa_{B_{l_o}}$	Component-dependent bending rigidity	$\kappa_{B_{l_o}} \approx (1.0-1.5)\times 10^{-19}$ J, $\kappa_{B_{l_d}} \approx (0.4-0.6)\times 10^{-19}$ J Evans & Rawicz (1990), Baumgart *et al.* (2005)
$\sigma_S(c_\Gamma)$	$\frac{1+c_\Gamma}{2}\sigma_{S_{l_d}} + \frac{1-c_\Gamma}{2}\sigma_{S_{l_o}}$	Component-dependent surface tension	Absolute $\sigma_{S_{l_o}}$ and $\sigma_{S_{l_d}}$ are not experimentally accessible; only effective tension can be measured(typically $10^{-8}-10^{-4}$ N m^{-1}). Evans & Rawicz (1990), Colom *et al.* (2018).
σ_L	—	Line tension	$10^{-13}-10^{-11}$ N Baumgart *et al.* (2003), Tian *et al.* (2007)
Dimensionless parameters			
Re	$\rho U L/\mu_{out}$	Reynolds number	—
Ca	$\mu_{out} U L^2/\kappa_{B_{l_o}}$	Bending capillary number	—
Pe	$L^2/(D_\phi \mu_{out})$	Péclet number for ϕ	—
Pen_Γ	$L/(D_c \mu_{out})$	Péclet number for c_Γ	—
Cn_Γ	$\sigma_L/(\mu_{out} U L)$	Line tension to viscous force ratio	—
Cs_Γ	$\sigma_{S_{l_o}}/(\mu_{out} U)$	Surface tension to viscous force ratio	—
κ_B	$\kappa_{B_{l_d}}/\kappa_{B_{l_o}}$	Bending rigidity contrast	—
σ_S	$\sigma_{S_{l_d}}/\sigma_{S_{l_o}}$	Membrane tension contrast	—
v	$3V/(4\pi(A/4\pi)^{3/2})$	Reduced volume ($v=1$ for sphere)	—
γ	$\dot{\gamma} L/U$	Dimensionless shear rate	—
Geometric parameter			
θ	$\in [-\pi/2, \pi/2]$	Inclination angle	—

Table 1. Physical and dimensionless parameters used in the simulations.

https://doi.org/10.1017/jfm.2026.11276 Published online by Cambridge University Press

approximation scheme multigrid algorithm and is specifically designed to address diffuse-interface problems (Guo *et al.* 2017). Within this framework, the velocity components $\boldsymbol{u} = (u, v, w)$ are stored at edge centres, while all scalar quantities, including pressure and phase-field variables, are stored at cell centres. Details of the spatial discretization can be found in Guo *et al.* (2017). Our simulations exhibit excellent qualitative and quantitative agreement with both experiments. These validations confirm the accuracy, effectiveness and predictive capability of the proposed model in capturing phase behaviours, vesicle–fluid coupling and dynamic transitions of multicomponent vesicles under shear flow.

3.1. *Phase separation on stationary multicomponent vesicles*

We first investigate phase separation dynamics on the membrane of multicomponent vesicles in comparison with the experimental results reported in Wang *et al.* (2022). That study examined the phase behaviour of GUVs and provided detailed observations of domain evolution. To facilitate a direct comparison, we simplify our set-up by assuming a stationary vesicle with a fixed spherical shape, focusing on capturing the essential features of membrane phase separation.

Here $\bar{\Omega} = [-1.5, 1.5]^3$ and is discretized using a uniform Cartesian grid of 128^3. The fixed spherical vesicle is represented by a phase-field with radius $r_0 = 1$, corresponding to a physical vesicle radius $R = 10\,\mu\text{m}$ (Wang *et al.* 2022), and membrane thickness $\varepsilon_\phi = 0.02$. The initial phase-field variable $\phi(\boldsymbol{x}, 0)$ is prescribed as

$$\phi(\boldsymbol{x}, 0) = \tanh\left(\frac{r_0 - r(\boldsymbol{x})}{2\sqrt{2}\varepsilon_\phi}\right), \quad r(\boldsymbol{x}) = \sqrt{x^2 + y^2 + z^2}, \quad \boldsymbol{x} = (x, y, z) \in \bar{\Omega}, \tag{3.1}$$

representing a smooth diffuse interface centred around the vesicle surface. To model an initially homogeneous liposome, we first generate random numbers $c_{rand}(\boldsymbol{x})$ with a uniform distribution between 0 and 1. Then, we apply the following cutoff for the initial surface fraction $c_\Gamma(\boldsymbol{x}, 0)$:

$$c_\Gamma(\boldsymbol{x}, 0) = \begin{cases} 1 \quad (l_d), & \text{if } c_{rand}(\boldsymbol{x}) \in [0, a_{l_d}], \\ -1 \quad (l_o), & \text{if } c_{rand}(\boldsymbol{x}) \in (a_{l_d}, 1], \end{cases} \tag{3.2}$$

where a_{l_d} and $a_{l_o} = 1 - a_{l_d}$ represent the prescribed area fractions of the l_d and l_o phases, respectively.

No-flux boundary conditions are applied to the phase-field variables ϕ, c_Γ and ω_c at the domain boundary $\partial\Omega$.

The model parameters are chosen to match those reported in Wang *et al.* (2022): line tension $\sigma_L = 1.2\,\text{pN}$ and diffusion coefficient $D_c = 10^{-5}\,\text{cm}^2\,\text{s}^{-1}$. The lipid mobility is adjusted such that $Cn_\Gamma/Pe_\Gamma = 0.12$. Bending rigidity and surface tension are assumed to be uniform across the l_o and l_d phases, with $\kappa_B = \sigma_S = 1$. The interfacial thickness of membrane components is set to $\varepsilon_c = 0.02$, fitted to match experimental GUVs.

Two area fractions, $a_{l_d} = 0.3$ and $a_{l_d} = 0.7$, are considered to match the experimental conditions in Wang *et al.* (2022). To account for stochastic variability, we perform 10 independent simulations with different random seeds of c_Γ for each area fraction.

Figures 2 and 3 show the phase separation process on the membrane for area fractions $a_{l_d} = 0.3$ and $a_{l_d} = 0.7$, respectively, compared with the experimental results from Wang *et al.* (2022). During phase separation, membrane components coarsen, forming distinct, stable domains, as illustrated in the rightmost images of both figures 2 and 3 that closely match the experimental snapshots.

https://doi.org/10.1017/jfm.2026.11276 Published online by Cambridge University Press

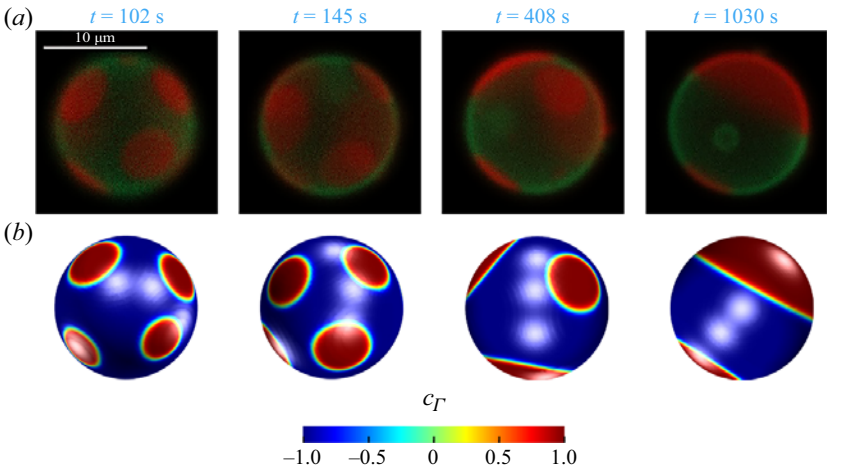


Figure 2. Phase separation on GUVs at $a_{l_d} = 0.3$: experimental snapshots (a) from Wang *et al.* (2022) and numerical results (b), showing l_o domains (blue) forming within the l_d phase (red).

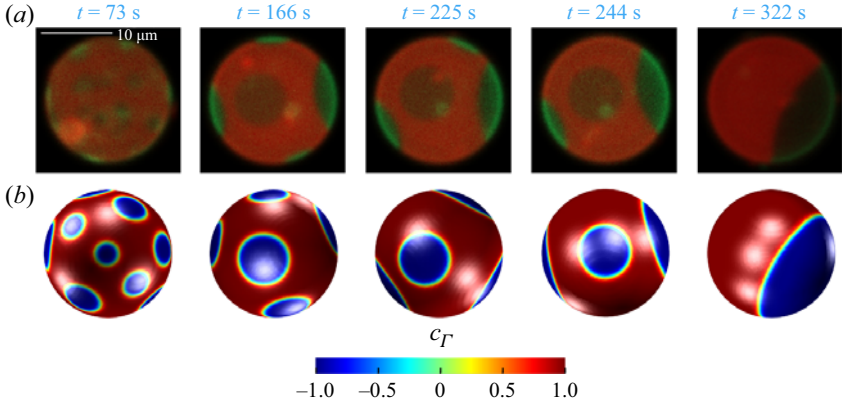


Figure 3. Phase separation on GUVs at $a_{l_d} = 0.7$: experimental snapshots (a) from Wang *et al.* (2022) and numerical results (b), showing l_d domains (red) forming within the l_o phase (blue).

To further validate the accuracy of our model, we compare the time evolution of the number of lipid domains obtained from our numerical simulations with the experimental measurements reported in Wang *et al.* (2022) (digitized using WebPlotDigitizer https://automeris.io/). In the simulations, lipid domains are identified directly on the membrane surface by extracting the isosurface $\phi = 0$, interpolating c_Γ onto this surface, thresholding at $c_\Gamma = 0$ and applying MATLAB's standard surface-connected-component labelling routine `bwconncomp` (https://www.mathworks.com/help/images/ref/bwconncomp.html.) As shown in figure 4, for both area fractions under investigation ($a_{l_d} = 0.3$ and $a_{l_d} = 0.7$), the experimental data (markers) are generally bounded by the minimum (green) and maximum (red) values from the ensemble of our simulations. The average numerical result (blue) also lies in close agreement with the experimental trend.

In addition, we further compare the evolution of the total perimeter of lipid domains, quantified by $\int_\Omega \zeta(\phi)\zeta(c_\Gamma)\,\mathrm{d}V$ in our simulations, where $\zeta(\phi)$ localizes the membrane and $\zeta(c_\Gamma)$ localizes the phase boundary, with the experimental data (digitized using WebPlotDigitizer), as shown in figure 5. The simulation results (solid lines), averaged

https://doi.org/10.1017/jfm.2026.11276 Published online by Cambridge University Press

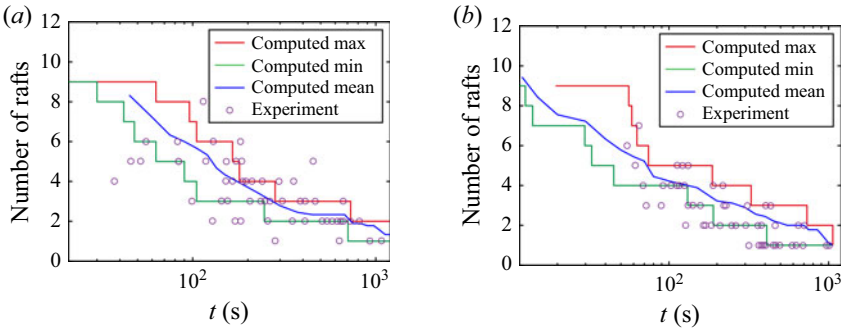


Figure 4. Time evolution of number of lipid rafts for $a_{l_d} = 0.3$ (a) and $a_{l_d} = 0.7$ (b). Markers represent experimental data; solid lines represent numerical results (blue, average; green, minimum; red, maximum).

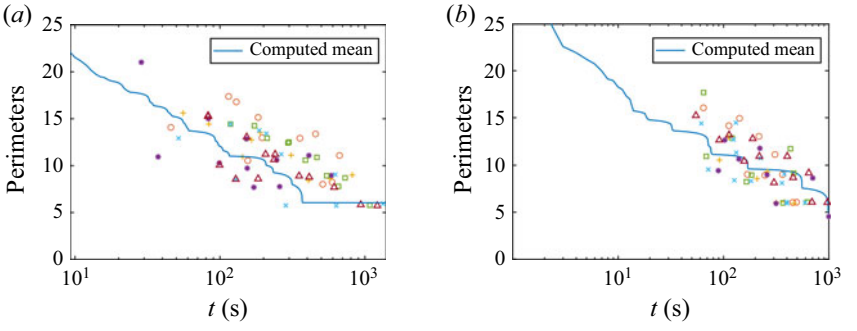


Figure 5. Time evolution of the total perimeter of lipid domains at $a_{l_d} = 0.3$ (a) and $a_{l_d} = 0.7$ (b). Markers represent experimental data; solid lines represent numerical results.

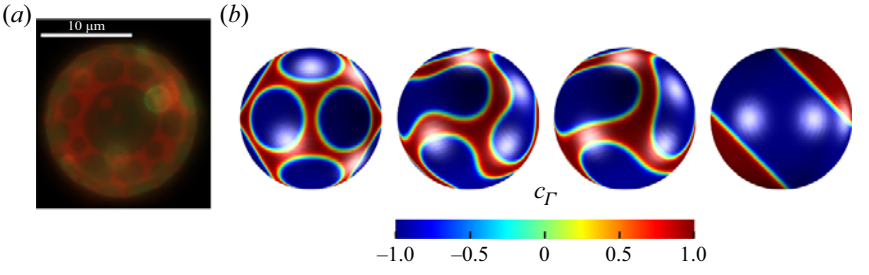


Figure 6. Experimental images (a) from Wang *et al.* (2022) and numerical results (b) showing the time evolution of l_o domains (blue) within the l_d phase (red). The simulation is initialized with 12 symmetrically placed l_o domains and an area fraction $a_{l_o} = 0.64$.

over all numerical simulations, exhibit excellent agreement with the experimental measurements (markers) for both $a_{l_d} = 0.3$ and $a_{l_d} = 0.7$.

As reported in Wang *et al.* (2022), three distinct structural patterns were observed experimentally at an area fraction of $a_{l_d} = 0.3$ prior to equilibrium: (i) the minority l_d phase domains (red) embedded within the majority l_o phase (blue), as shown in figure 2; (ii) majority l_o phase domains (blue) enclosed within the minority l_d phase (red), as illustrated in figure 6; and (iii) a mixed pattern featuring both types of domains, as depicted in figure 7.

https://doi.org/10.1017/jfm.2026.11276 Published online by Cambridge University Press

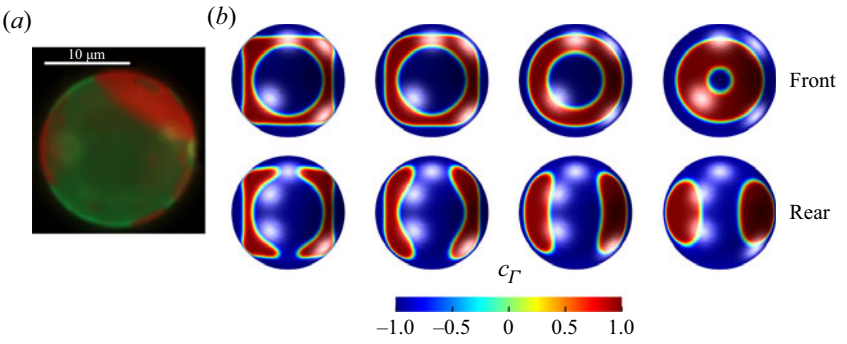


Figure 7. Experimental images (*a*) from Wang *et al.* (2022) and numerical results (*b*) with front and rear views over time, showing a combination of l_o phase (blue) and l_d phase (red). The simulation is initialized with six symmetrically placed l_o domains and an area fraction $a_{l_o} = 0.65$.

Patterns (ii) and (iii) were attributed to the persistence of a metastable third phase, which influences domain coarsening and leads to fluctuations in domain area fractions before equilibrium (Van Santen 1984; Anderson & Lekkerkerker 2002). For instance, the measured l_o area fraction in case (ii) was approximately 6 % lower than its equilibrium value.

Following Wang *et al.* (2022), we reproduce the experimentally observed patterns by adjusting the initial conditions: (i) prescribing prepositioned, symmetrically arranged l_o domains within an l_d background, and (ii) reducing the l_o area fraction by approximately 6 %. Accordingly, the second pattern – l_o domains fully enclosed within the l_d phase (figure 6) – is reproduced by initializing 12 symmetrically placed l_o domains with an area fraction $a_{l_o} = 0.64$. The third pattern, featuring coexisting l_o and l_d domains (figure 7), is obtained by initializing six symmetrically distributed l_o domains and setting $a_{l_o} = 0.65$.

The quantitative and qualitative agreement between our reproduced simulations and the experimental observations demonstrates the effectiveness and accuracy of our model in capturing the phase dynamics associated on the vesicle membrane.

3.2. *Dynamics of a two-component vesicle under shear flow*

To assess the capability of the model in capturing membrane–fluid interactions, we reproduce the experimental observations of multicomponent GUVs under shear flow reported in Tusch *et al.* (2018). These experiments revealed dynamic behaviours such as tank treading, swinging and tumbling, driven by asymmetric phase distributions and periodic elastic energy storage along the contact line.

In our simulations, $\bar{\Omega} = [-2, 2]^3$, discretized on a uniform grid with 128^3. To match the experimental set-up, the initial vesicle shape is modelled as a prolate ellipsoid with a specified reduced volume. The initial phase variable is given by

$$\phi(\boldsymbol{x}, 0) = \tanh\left(\frac{r_0 - r(\boldsymbol{x})}{2\sqrt{2}\varepsilon_\phi}\right), \quad r(\boldsymbol{x}) = \sqrt{\frac{x^2}{d_1^2} + \frac{y^2}{d_2^2} + \frac{z^2}{d_3^2}}, \quad \boldsymbol{x} = (x, y, z) \in \bar{\Omega}, \tag{3.3}$$

where $d_1 > d_2 = d_3$, resulting in elongation along the X-axis (see figure 8). The membrane component c_Γ is initially prepositioned at the tips of the vesicle along the X-axis, with a prescribed area fraction a_{l_d} representing the fraction of the l_d phase.

The shear flow is introduced by imposing boundary conditions. Specifically, Dirichlet boundary conditions $\boldsymbol{u}_{bc} = (\gamma z, 0, 0)$ are imposed at the top and bottom boundaries in the z-direction, where γ denotes the dimensionless shear rate (see table 1). No-flux boundary

https://doi.org/10.1017/jfm.2026.11276 Published online by Cambridge University Press

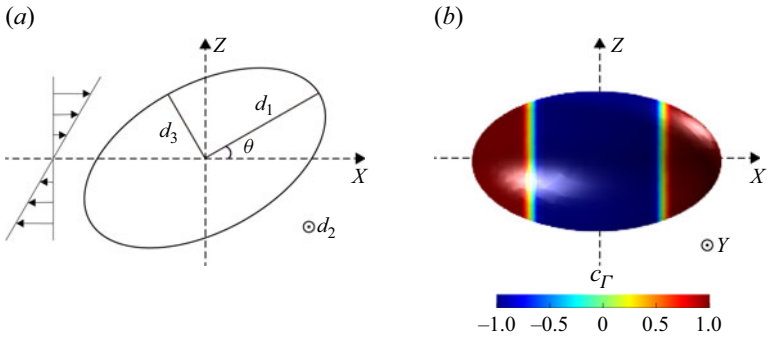


Figure 8. (*a*) Geometric parameters used to characterize vesicle dynamics under shear flow. The vesicle shape is described by its principal semiaxes (d_1, d_2, d_3), and the inclination angle θ is defined as the angle between the major axis d_1 and the flow direction (X-axis). (*b*) Initial phase distribution used in the simulations of § 4, shown in the X–Z view.

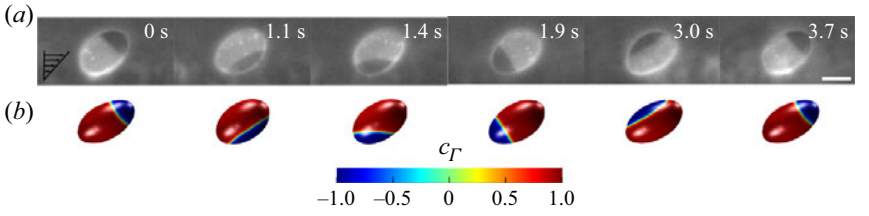


Figure 9. Experimental images (*a*) from Tusch *et al.* (2018) and numerical results (*b*) showing tank treading and swinging at $Cn_\Gamma = 8$, for a vesicle with reduced volume $v = 0.95$, flattening $f = 0.3$ and area fraction $a_{l_d} = 0.7$.

conditions are enforced for all phase-field variables (ϕ, ω_ϕ, c_Γ, ω_c) in the z-direction, while periodic boundary conditions are applied in the x- and y-directions for all variables.

Physical parameters are mainly taken from Tusch *et al.* (2018): mean vesicle radius $R = 10\,\mu$m, fluid viscosity $\mu_{in} = \mu_{out} = 1.2 \times 10^{-3}$ Pa s, bending rigidity $\kappa_{B_{l_o}} = \kappa_{B_{l_d}} = 10^{-19}$ J and shear rate $\dot{\gamma} = 3\,\mathrm{s}^{-1}$. Fluid densities are taken as $\rho_{in} = \rho_{out} = 1000\,\mathrm{kg\,m}^{-3}$ (Luby-Phelps 1999*b*). Surface tensions are fixed at $\sigma_{S_{l_d}} = \sigma_{S_{l_o}} = 10^{-6}\,\mathrm{N\,m}^{-1}$ to ensure uniform membrane properties. The line tension σ_L is varied as 4, 1 and 0.1 pN to reproduce the three dynamical regimes observed experimentally.

Using R as the characteristic length and $\dot{\gamma}R$ as the velocity scale, the resulting dimensionless parameters are Reynolds number $Re = 3 \times 10^{-4}$, bending capillary number $Ca = 36$, Péclet numbers $Pe = 1000$ and $Pe_\Gamma = 10$, dimensionless surface tension strength $Cs_\Gamma = 27$ and surface area penalty coefficient $\mathcal{M}_S = 2000$. The Cahn number is set as $Cn_\Gamma = 8,\ 2,\ 0.2$ for the three regimes (figures 9–11). Interfacial thickness parameters $\varepsilon_c = 0.05$ for membrane components and $\varepsilon_\phi = 0.05$ for the membrane are fitted to experimental GUVs.

Figures 9–11 illustrate vesicle dynamics under different reduced volumes, showing close agreement with the experimental results from Tusch *et al.* (2018). In figure 9, the initial ellipsoid with $d_1 = 1$, $d_2 = d_3 = 0.7$, yields $v \approx 0.95$, flattening parameter $f = (d_1 - d_2)/d_1 = 0.3$ and area fraction $a_{l_d} = 0.7$. At $Cn_\Gamma = 8$, the vesicle exhibits tank treading and swinging characterized by a steady prolate shape with oscillatory inclination angle.

At a moderate reduced volume $v \approx 0.8$, shown in figure 10, with $d_1 = 1$, $d_2 = d_3 = 0.35$, $f = 0.65$ and $a_{l_d} = 0.6$, the vesicle exhibits pronounced deformation at $Cn_\Gamma = 2$. It appears elliptical when the l_o–l_d interface aligns with the short axis and resembles two

https://doi.org/10.1017/jfm.2026.11276 Published online by Cambridge University Press

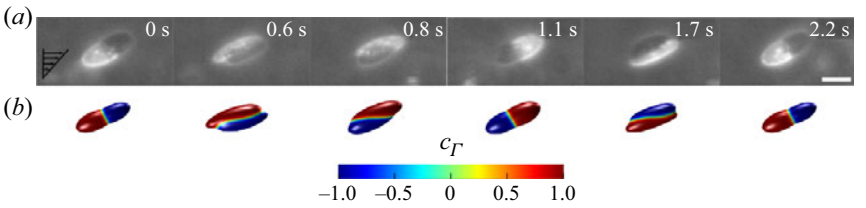


Figure 10. Experimental images (*a*) from Tusch *et al.* (2018) and numerical results (*b*) showing strong deformation during tank treading and swinging at $Cn_\Gamma = 2$, for a vesicle with reduced volume $v = 0.8$, flattening parameter $f = 0.65$ and area fraction $a_{l_d} = 0.6$.

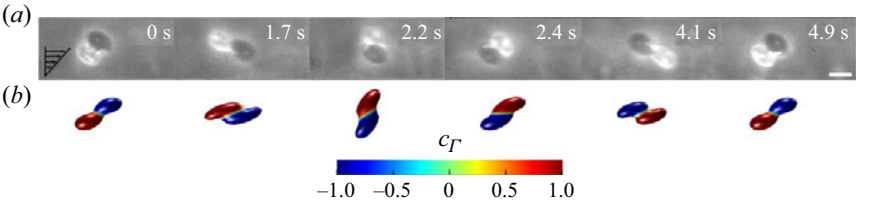


Figure 11. Experimental images (*a*) from Tusch *et al.* (2018) and numerical results (*b*) showing the tumbling at $Cn_\Gamma = 0.2$, for a vesicle with reduced volume $v = 0.7$, flattening parameter $f = 0.75$ and area fraction $a_{l_d} = 0.5$.

adhered vesicles when aligned with the long axis, exhibiting tank treading and swinging accompanied by large deformations.

At lower volume $v \approx 0.7$ (figure 11), with $d_1 = 1$, $d_2 = d_3 = 0.25$, $f = 0.75$ and $a_{l_d} = 0.5$, the vesicle transitions to a tumbling regime at $Cn_\Gamma = 0.2$. The interface length between l_o and l_d is markedly reduced along the long axis due to line tension, which drives the system to minimize line energy, facilitating large deformations and promoting tumbling under shear.

To further validate our model, we track the time evolution of the inclination angle θ of a vesicle undergoing tank treading and swinging behaviours at reduced volume $v = 0.95$ and area fraction $a_{l_d} = 0.7$ (see figure 9). The inclination angle θ is defined as the angle between the vesicle's long axis and the flow direction, constrained within $\theta \in [-\pi/2, \pi/2]$ (see figure 8). As shown in figure 12, the simulated results (solid line) closely match the experimental measurements (circles) reported in Tusch *et al.* (2018) (digitized using WebPlotDigitizer), capturing the characteristic oscillations of the tank treading and swinging regime with a mean angle of approximately 30°. The numerical results remain consistently within the experimental variability, thereby confirming not only the accuracy and robustness of the model but also its predictive capability in reproducing flow-induced vesicle dynamics.

4. Numerical experiments

In this section, we investigate the flow-induced dynamics of multicomponent vesicles, with a particular focus on the coupling between membrane heterogeneity and hydrodynamic forces. Through comprehensive numerical simulations, we demonstrate that the competition among shear flow, bending rigidity heterogeneity and surface tension heterogeneity governs complex vesicle behaviours, including shape deformation, domain evolution and transitions between distinct dynamic regimes.

https://doi.org/10.1017/jfm.2026.11276 Published online by Cambridge University Press

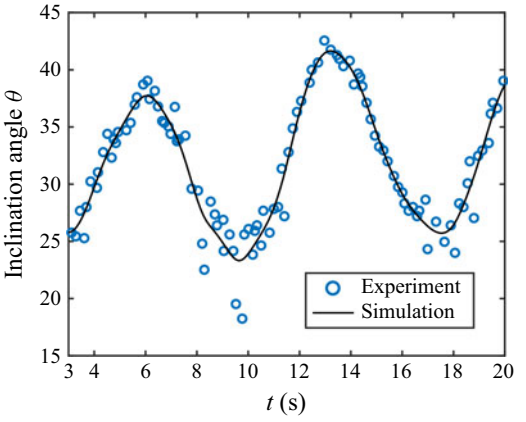


Figure 12. Time evolution of inclination angle θ for a vesicle with reduced volume $v = 0.95$, flattening parameter $f = 0.3$ and area fraction $a_{l_d} = 0.7$ at $Cn_\Gamma = 8$, comparing numerical results (solid line) with experimental data (circles) from Tusch *et al.* (2018).

4.1. *Bending heterogeneity-driven dynamics*

We systematically explore the coupling between shear flow and bending heterogeneity in multicomponent vesicles by varying the bending rigidity contrast $\kappa_B = \kappa_{B_{l_d}}/\kappa_{B_{l_o}}$ and the bending capillary number $Ca = \mu_{out} U L^2/\kappa_{B_{l_o}}$, both readily tuneable in experiments.

The numerical set-up closely follows § 3.2. The vesicle is initialized as a prolate ellipsoid with principal axes $d_1 = 1$ and $d_2 = d_3 = 0.565$, as defined in (3.3), corresponding to a reduced volume $v \approx 0.91$. Two symmetric l_d-phase domains (red) are prepositioned at the vesicle tips along the X-axis (see figure 8), with an initial area fraction $a_{l_d} = 0.4$ for the membrane component field c_Γ. The dimensionless shear rate is set to $\gamma = 1$.

Moreover, the dimensionless parameters are specified as follows: Reynolds number $Re = 10^{-3}$; Cahn number $Cn_\Gamma = 0.05$; Péclet numbers $Pe = 1000$ and $Pe_\Gamma = 1$; dimensionless surface-tension strength $Cs_\Gamma = 10$; surface-area penalty coefficient $\mathcal{M}_S = 2000$; surface tension contrast $\sigma_S = 1$. In all cases, the l_d phase is assumed to be softer than the l_o phase, i.e. $\kappa_{B_{l_d}} < \kappa_{B_{l_o}}$.

Figure 13 presents a phase diagram spanned by (κ_B, Ca), capturing diverse dynamics of multicomponent vesicles and identifying six distinct dynamical regimes.

(i) Lateral ring banding. The vesicle adopts an oblate, tilted shape, with l_d phase domains stretching along the edges to form a lateral ring band composed of a single slender domain.
(ii) Lateral broken-ring banding. Similar to (I), but the l_d phase domains form a broken lateral ring composed of two slender domains.
(iii) Tank treading. The vesicle assumes a prolate, tilted shape, with l_d phase domains stably located at the high-curvature tips (reported in Liu *et al.* (2017) and Venkatesh & Narsimhan (2024)).
(iv) Vertical broken-ring banding. The l_d phase domains stretch vertically along the flow direction on the membrane of a prolate, tilted vesicle. This results in a vertical broken ring composed of two slender domains.
(v) Vertical ring banding. Similar to (IV), but the l_d phase domains merge into a complete vertical ring band composed of a single slender domain (reported in Gera & Salac (2018*b*)).

https://doi.org/10.1017/jfm.2026.11276 Published online by Cambridge University Press

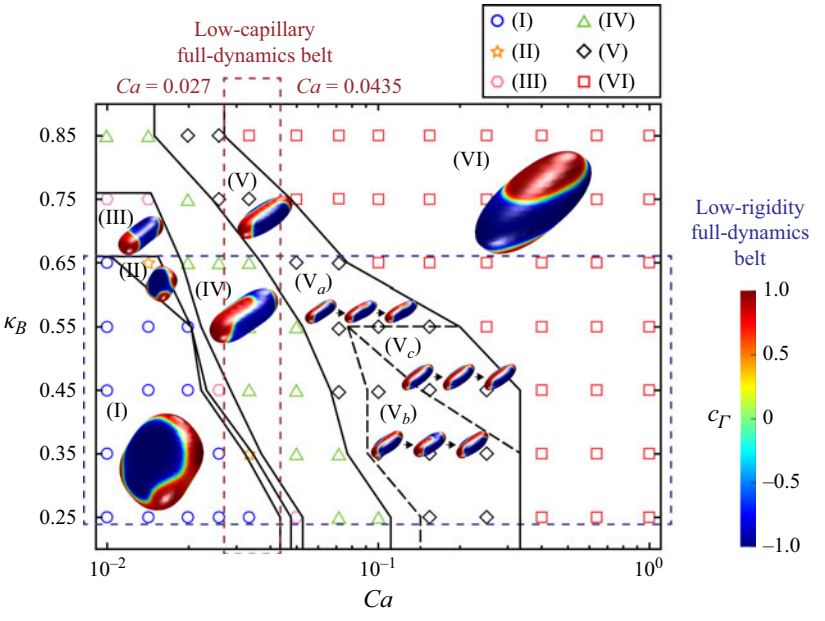


Figure 13. Phase diagram of vesicle dynamics under shear flow as a function of bending rigidity contrast κ_B and capillary number Ca. Regimes (I)–(VI) are distinguished by colours and markers.

(vi) Phase treading. The l_d phase domains migrate periodically along the membrane of a prolate, tilted vesicle from one tip to the other tip in the flow direction, while maintaining the initial domain symmetry (reported in Liu *et al.* (2017), Gera & Salac (2018*b*) and Venkatesh & Narsimhan (2024)).

Note that, regimes (I), (II) and (IV) have not been previously reported and represent novel dynamical regimes driven by membrane bending heterogeneity under shear flow.

The phase diagram also reveals two prominent 'dynamical belts': (i) a 'low-rigidity full-dynamics belt' ($0.25 \leq \kappa_B \leq 0.65$), where the membrane rigidity contrast is small enough for all six regimes to appear across a wide range of Ca; and (ii) a 'low-capillary full-dynamics belt' ($0.027 \lesssim Ca \lesssim 0.043$), where relatively weak shear allows all six regimes to emerge over a range of κ_B.

Within the 'low-rigidity full-dynamics belt' ($0.25 \leq \kappa_B \leq 0.65$), increasing Ca drives a flow-mediated transition pathway through the dynamical regimes: at low Ca, weak shear and dominant bending energy lead the vesicle to adopt an oblate shape, with low-rigidity l_d domains accumulating along high-curvature lateral edges, forming (I) lateral ring banding. As Ca increases moderately, enhanced shear stresses partially rupture the l_d domains at the lateral edges, producing (II) lateral broken-ring banding. With further increase in Ca, the vesicle elongates into a prolate shape, and the l_d domains stabilize at the high-curvature tips, resulting in (III) tank treading. At higher Ca, the l_d domains stretch vertically along the membrane, but insufficient membrane fluidity prevents full closure into a ring, resulting in (IV) vertical broken-ring banding. At sufficiently high Ca, the l_d domains are further stretched and coalesce into (V) vertical ring banding. Under even stronger Ca, persistent and periodic domain migration emerges, characterized by symmetric phase migration, known as (VI) phase treading.

Outside the 'low-rigidity full-dynamics belt' ($\kappa_B > 0.65$), the diversity of accessible dynamical regimes progressively narrows. For $0.65 \leq \kappa_B < 0.75$, only regimes (III)–(VI)

https://doi.org/10.1017/jfm.2026.11276 Published online by Cambridge University Press

remain, while for $\kappa_B > 0.75$, regime (III) also vanishes. This reduction in dynamical regimes results from the diminishing bending-rigidity contrast between the l_d and l_o phases, which weakens the tendency of low rigidity l_d domains to localize at high-curvature regions and suppresses bending-driven behaviours such as (I) lateral ring banding.

Notably, within the 'low-capillary full-dynamics belt' ($0.027 \leq Ca \lesssim 0.0435$) shown in figure 13, we observe a complete sequence of transitions from regime (I) to regime (VI) as κ_B increases. This highlights the strong sensitivity of both domain and shape evolution to bending rigidity contrast under moderate shear, and identifies this belt as a critical parameter space for capturing diverse vesicle dynamical regimes.

We further observe that the critical capillary numbers separating successive regimes-for example, the transition from (IV) to (V) – generally decrease with increasing κ_B, except for the (V) to (VI) transition at $\kappa_B \leq 0.45$. This trend indicates that stronger flow is typically required to induce domain migration and evolution under pronounced bending heterogeneity, reflecting a competition between shear-induced forces and membrane bending rigidity contrast.

Moreover, within the (V) vertical ring banding regime in figure 13, we identify three subregimes based on ring dynamics.

- (V_a) Temporary ring. The l_d domains briefly merge into a vertical ring that ruptures and stabilizes into a broken-ring configuration.
- (V_b) Cyclic broken and closing ring. The l_d domains repeatedly merge into a vertical ring that undergoes persistent cycles of rupture and reconnection.
- (V_c) Stable ring. The l_d domains experiences several rupture-reconnect cycles but eventually stabilizes and remains intact over long times.

These subregimes emerge from transitions driven by the bending heterogeneity κ_B and capillary number Ca. At $\kappa_B \geq 0.65$, a weak bending heterogeneity reduces the preference of l_d domains for high-curvature tips, restricting dynamics to (V_a). For $0.45 < \kappa_B < 0.65$, increasing Ca triggers sequential transitions from (V_a) to (V_b) and ultimately to (Vc). At $\kappa_B \leq 0.45$, a strong heterogeneity destabilizes the ring, suppressing (V_c). Notably, (V_a) is distinct from regime (IV): in (V_a), a transient ring forms and then ruptures, whereas in (IV), the l_d domains never coalesce into a ring.

Figure 14 illustrates six distinct vesicle dynamic regimes (I)–(VI) at $\kappa_B = 0.65$ within the 'low-rigidity full-dynamics belt'. Figure 14(a) shows their temporal evolution (see supplementary Movie-1, Movie-2, Movie-3, Movie-4, Movie-5 and Movie-6, corresponding to regimes (I)–(VI), respectively), are available at https://doi.org/10.1017/jfm.2026.11276, while figure 14(b) presents the corresponding bending and line energy profiles from $t = 2$ to $t = 38$. To capture the key dynamical processes, we mark the critical turning points (t_i for $i = 1, \ldots, 9$, see the caption of figure 14) on the energy curves. These turning points of bending and line energies largely coincide.

Comparing the l_d phase domain positions in figure 14(a) with the energy evolution in figure 14(b) provides valuable insights into vesicle dynamics. In regimes (I)–(III), l_d domains (with lower rigidity $\kappa_{B_{l_d}}$) localize at high-curvature regions, minimizing bending energy and resulting in similar energy levels. However, due to the relatively low Ca, bending forces dominate over viscous forces, preventing further reduction in line energy. In regime (IV), the l_d domains stretch from the high-curvature tips towards low-curvature regions away from the tips, leading to a temporary increase in bending energy from t_1 to t_3. Unable to overcome the energy barrier required to form a vertical ring, both the bending and line energies stabilize thereafter at t_7. In regime (V), the l_d domains initially stretch towards low-curvature membrane regions away from the tips, increasing bending and line

https://doi.org/10.1017/jfm.2026.11276 Published online by Cambridge University Press

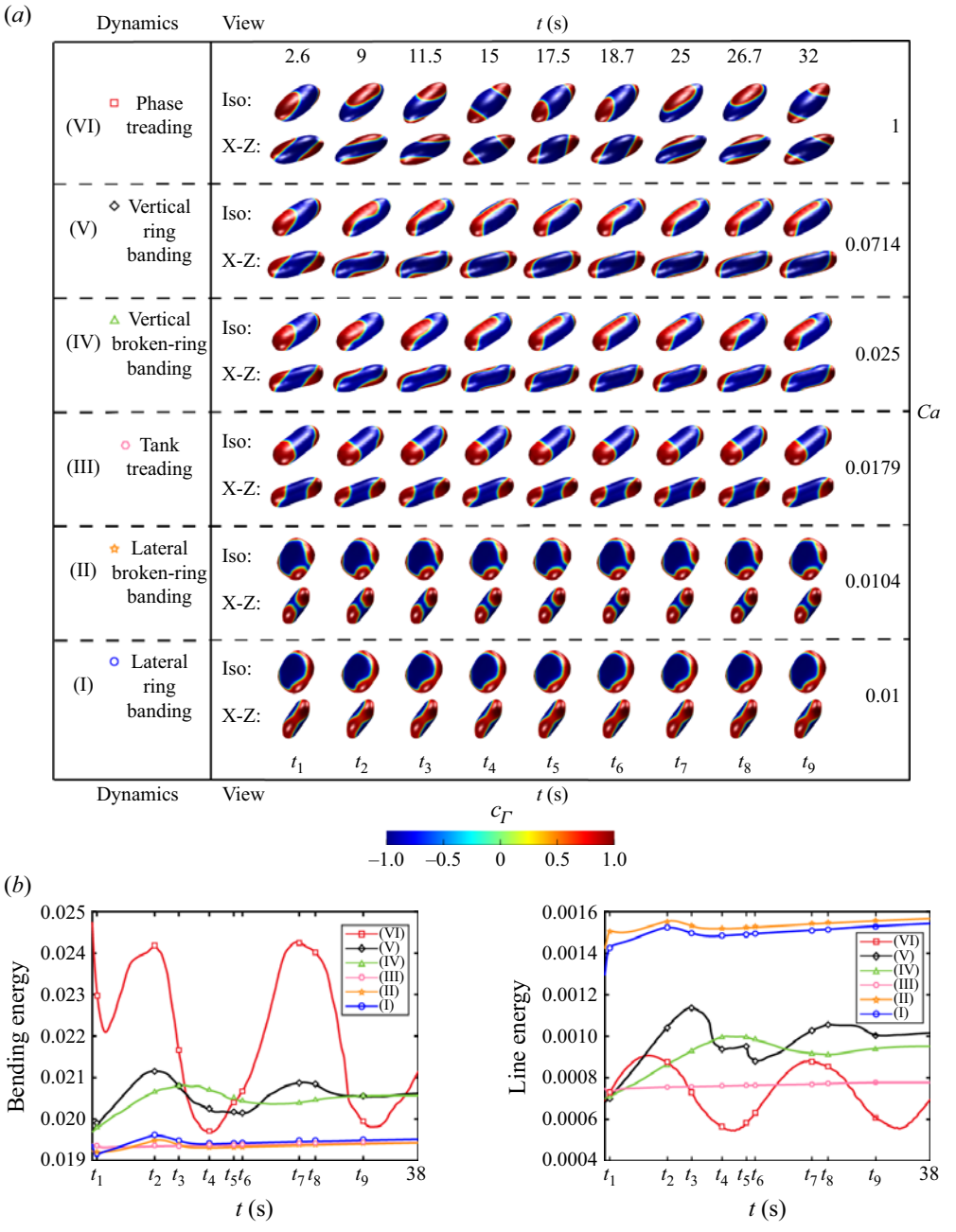


Figure 14. (*a*) Time evolution of six vesicle dynamic regimes (I)–(VI) at $\kappa_B = 0.65$ with varying *Ca*. (*b*) Corresponding evolution of bending and line energies. Key time points: $t_1 = 2.6$, $t_2 = 9$, $t_3 = 11.5$, $t_4 = 15$, $t_5 = 17.5$, $t_6 = 18.7$, $t_7 = 25$, $t_8 = 26.7$, $t_9 = 32$.

energies from t_1 to t_2. At t_4, the domains merge into a vertical ring band, minimizing both energies. After t_9, the domains stabilize into a broken-ring configuration. Strictly, this case at $\kappa_B = 0.65$ corresponds to subregime (V_a), with detailed subregime dynamics presented in figure 15. In (VI), l_d domains periodically migrate along the membrane. Bending energy

https://doi.org/10.1017/jfm.2026.11276 Published online by Cambridge University Press

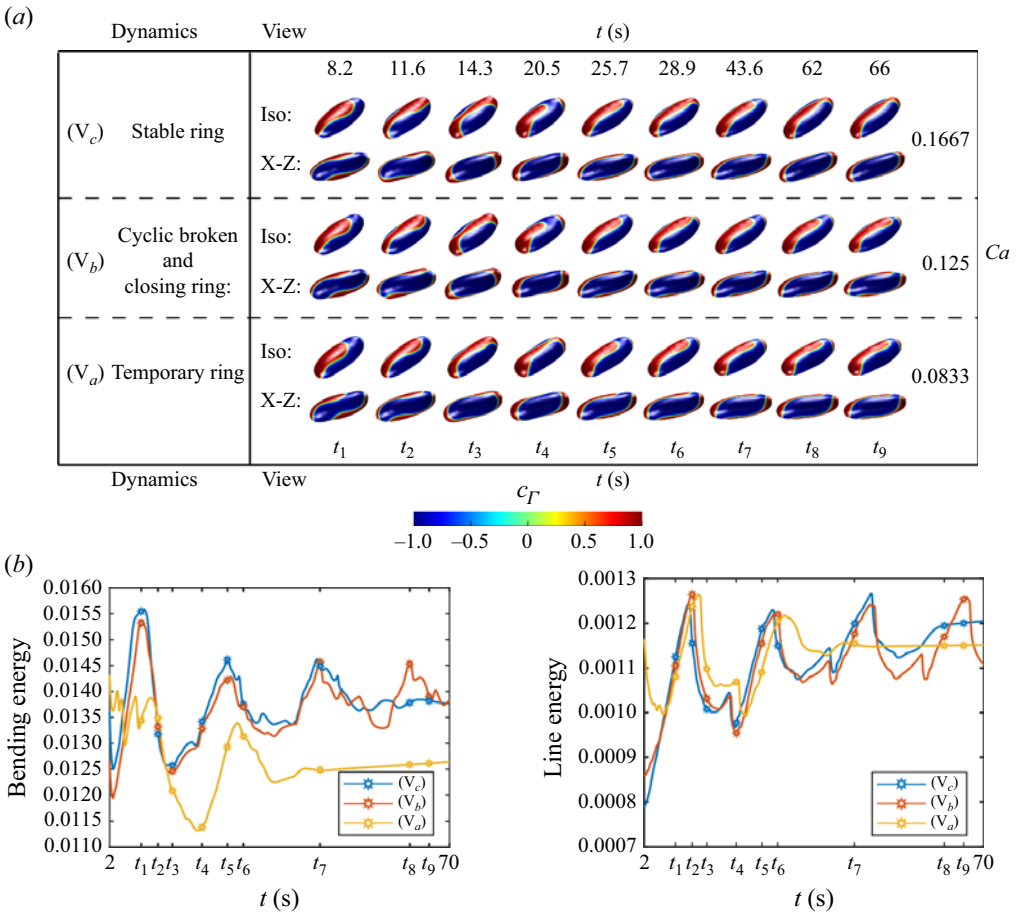


Figure 15. (*a*) Time evolution of subregimes (V_a)–(V_c) within regime **(V)** at $\kappa_B = 0.45$ with varying *Ca*. (*b*) Corresponding evolution of bending and line energies. Key time points: $t_1 = 8.2$, $t_2 = 11.6$, $t_3 = 14.3$, $t_4 = 20.5$, $t_5 = 25.7$, $t_6 = 28.9$, $t_7 = 43.6$, $t_8 = 62$, $t_9 = 66$.

peaks when domains align along flatter regions (e.g. t_2, t_7) and decreases when they reach high-curvature tips (e.g. t_4, t_9).

To further investigate the (V) vertical ring banding regime, figure 15 presents three subregimes: (V_a), (V_b) and (V_c). Figure 15(*a*) shows the temporal evolution of each dynamics subregime, while figure 15(*b*) shows the corresponding bending and line energies from $t = 2$ to $t = 70$, with key transition points (t_i, $i = 1, \ldots, 9$, see the caption of figure 15) marked. Consistent with figure 14, the l_d phase domain positions correlate with energy evolution. We find that the three subregimes exhibit similar energy evolution before t_4, as all initially form a vertical ring. Subsequent divergence arises from differences in l_d domain evolution. In (V_a), the ring ruptures and stabilizes as a broken-ring after t_7, with both bending and line energies reaching stability. In (V_b), the ring undergoes periodic rupture–reconnection, leading to cyclic oscillations of the energy: bending energy increases during rupture (e.g. t_3 to t_4) as more low-rigidity l_d domains migrate to low-curvature regions away from the tips, and decreases during reconnection (e.g. t_5 to t_6). In (V_c), after two rupture–reconnection cycles (from t_3 to t_8), the l_d domains form a stable vertical ring at t_8, with both bending and line energies stabilizing thereafter. Notably, the

https://doi.org/10.1017/jfm.2026.11276 Published online by Cambridge University Press

equilibrium energies in (V_c) are higher than in (V_a) due to (i) a larger fraction of low-rigidity l_d domains remaining in low-curvature regions, increasing bending energy and (ii) a longer l_d-l_o interface, elevating line energy.

4.2. *Surface tension heterogeneity-driven swinging and tumbling*

We next investigate the role of membrane surface tension heterogeneity $\sigma_S = \sigma_{S_{l_d}}/\sigma_{S_{l_o}}$ in modulating vesicle dynamics under shear flow. Within the 'low-rigidity full-dynamics belt' at a fixed bending rigidity contrast $\kappa_B = 0.65$, we systematically vary $\sigma_S \leq 1$ and the bending capillary number Ca.

The numerical set-up follows § 4.1. In all cases, the l_d phase is assumed to possess lower surface tension than the l_o phase, i.e. $\sigma_{S_{l_d}} < \sigma_{S_{l_o}}$.

The phase diagram (figure 16) reveals eight dynamical regimes: the six previously identified (I–VI) and two additional regimes.

(vii) Swinging. Small-amplitude oscillations of the vesicle inclination angle, coupled with cyclic rupture and reconnection of the l_d-formed vertical ring, similar to (V_b).
(viii) Tumbling. Rigid-body-like vesicle rotation, with l_d domains stably anchored at high-curvature tips.

Swinging and tumbling dynamics have been previously reported in single-component vesicles with viscosity contrast, and in multicomponent vesicles with small-deformation bending heterogeneity (Gera *et al.* 2022; Venkatesh & Narsimhan 2024) or with shape asymmetry arising from initial phase distributions and bending heterogeneity (Liu *et al.* 2017). Here, we identify a novel mechanism: surface tension heterogeneity, without viscosity contrast or asymmetric phase distributions, can also induce swinging and tumbling. As shown in figure 16, regimes (VII) and (VIII) occur only under heterogeneous surface tension ($\sigma_S < 1$).

Under uniform surface tension ($\sigma_S = 1$), moderate capillary numbers ($0.0189 \lesssim Ca \lesssim 0.037$) drive the vesicle into regime (IV), characterized by vertical broken-ring banding. As σ_S decreases to 0.85, enhanced membrane fluidity enables l_d domains to overcome the energy barrier, forming a complete ring. Periodic rupture and reconnection of this vertical ring dynamically alter the inclination angle, resulting in regime (VIII). At high capillary numbers ($0.037 \lesssim Ca \leq 1$), uniform surface tension ($\sigma_S = 1$) induces regimes (V), characterized by vertical ring banding, and (VI), defined by phase treading. As σ_S decreases to 0.85, regime (VIII) tumbling emerges. This transition occurs because the lower-tension l_d domains become strongly anchored at the high-curvature tips, suppressing their migration and introducing hydrodynamic asymmetry that promotes rigid-body-like rotation.

Overall, decreasing σ_S lowers the energetic cost of deforming l_d domains, enhancing their mobility and reducing the critical capillary number Ca required for successive dynamic regime transitions. As a result, at $0.85 \leq \sigma < 1$ only regimes (II)–(IV), (VII) and (VIII) persist, regime (I) becomes unsustainable under shear, while swinging and tumbling emerge as the dominant dynamic responses. In addition, for $0.35 \leq \sigma_S < 0.85$, only regimes (II), (III) and (VIII) persist. In this range, strong surface tension contrast firmly anchors l_d domains at the tips, promoting vesicle rotation and lowering the threshold for tumbling, while suppressing other regimes as domain evolution rapidly stabilizes. When $\sigma_S < 0.35$, only (VIII) is observed across all tested Ca, indicating that extreme surface tension asymmetry robustly favours rigid-body-like rotation.

https://doi.org/10.1017/jfm.2026.11276 Published online by Cambridge University Press

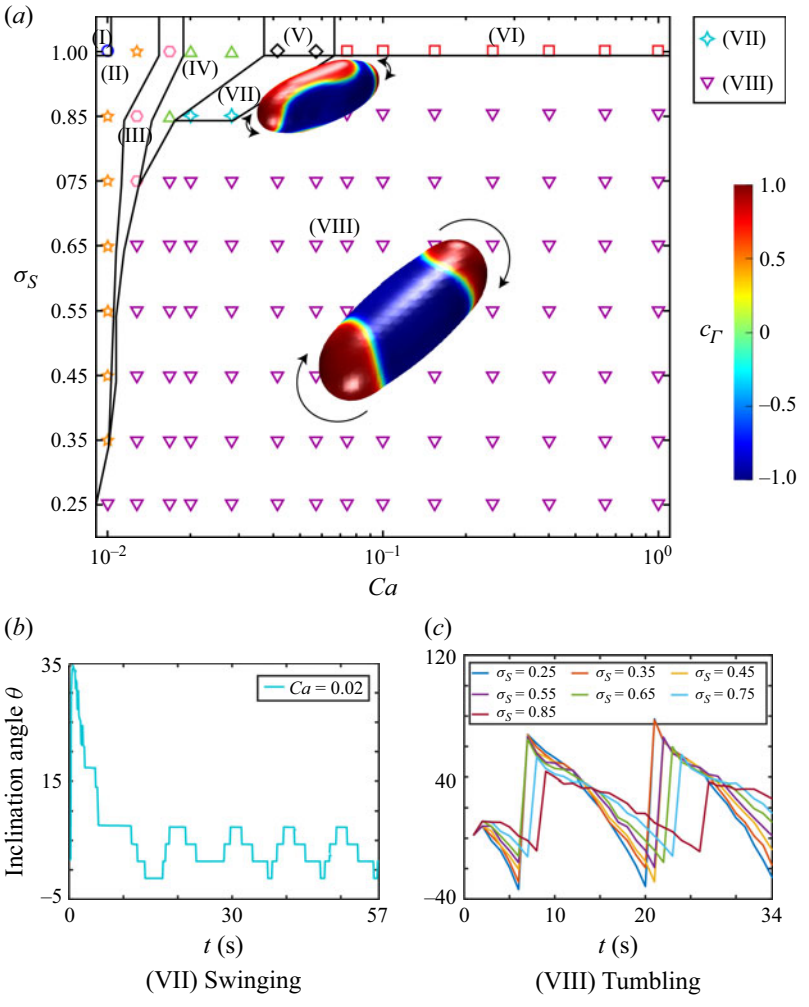


Figure 16. (*a*) Phase diagram of vesicle dynamics under shear flow as a function of surface tension contrast σ_S and capillary number Ca at fixed bending rigidity contrast $\kappa_B = 0.65$. Eight dynamic regimes (I)–(VIII) are identified and distinguished by colours and markers. (*b*) Inclination angle evolution in regime (VII) at $\sigma_S = 0.85$, $Ca = 0.02$. (*c*) Inclination angle evolution in regime (VIII) at $Ca = 1$ for varying σ_S.

The distinct signatures of (VII) swinging and (VIII) tumbling are further quantified in figure 16(*b*), which show the time evolution of the vesicle inclination angle for regimes (VII) and (VIII). In (VII) Swinging, the angle exhibits step-like segments linked to the rupture and reconnection of the l_d ring. As l_d domains stretch towards low-curvature regions, surface tension gradients reduce the inclination angle; after rupture, domains shift back to the tips, increasing the angle. These non-smooth variations reflect the interplay between domain evolution and shear force. In (VIII) tumbling, further decreasing σ_S at a fixed Ca accelerates the angular rotation, driven by stronger surface tension gradients.

In addition, figure 17 provides a comprehensive depiction of the (VII) swinging and (VIII) tumbling regimes. Figure 17(*a*) illustrates their temporal evolution (see supplementary Movie-7 and Movie-8, corresponding to regimes (VII)–(VIII), respectively), while figure 17(*b*) presents the corresponding bending, line and surface energies starting from $t = 2$ to $t = 40$. The critical time points (t_i, for $i = 1, \ldots, 9$; see caption of figure 17) are

https://doi.org/10.1017/jfm.2026.11276 Published online by Cambridge University Press

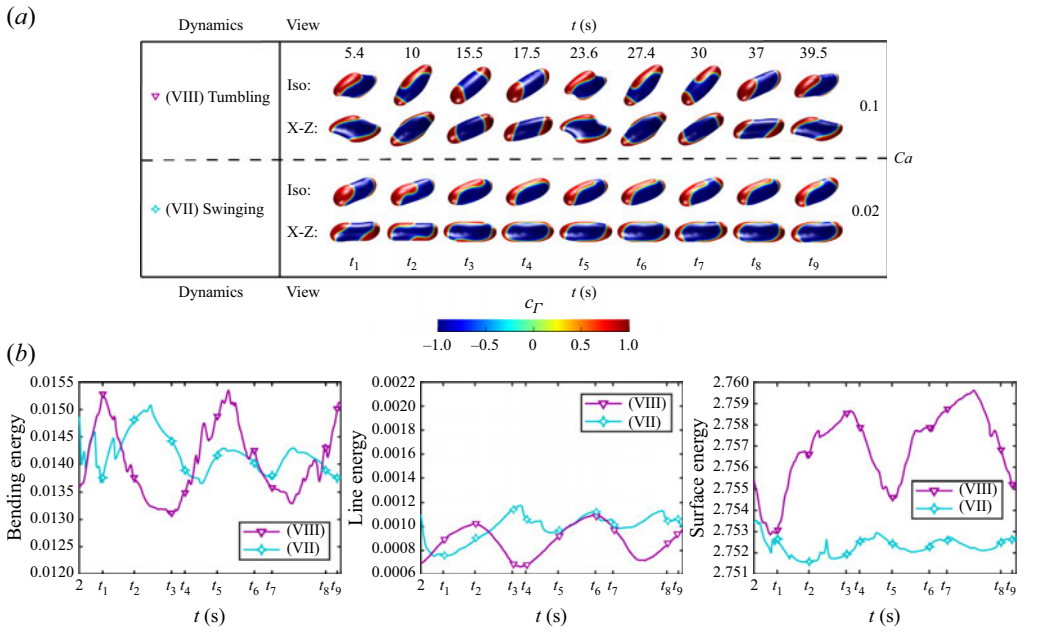


Figure 17. (*a*) Time evolution of vesicle dynamic regimes (VII) and (VIII) at $\sigma_S = 0.85$ and $\kappa_B = 0.65$. (*b*) Corresponding evolution of bending, line and surface energies. Key time points: $t_1 = 5.4$, $t_2 = 10$, $t_3 = 15.5$, $t_4 = 17.5$, $t_5 = 23.6$, $t_6 = 27.4$, $t_7 = 30$, $t_8 = 37$, $t_9 = 39.5$.

marked on the energy curves. The evolution of bending and line energies, which reflects the migration of l_d domains, is consistent with the discussion in § 4.1 and is not repeated here. The following analysis focuses on the variations in surface energy.

In (VII) swinging, as shown in figure 17(*a*), periodic rupture and reconnection of the ring cause surface energy to oscillate. When the ring reconnects, l_d domains stretch into low-curvature regions, increasing both their area and the surface energy (e.g. around t_4). When the ring ruptures, l_d domains cluster near the high-curvature tips, reducing their area and lowering surface energy (e.g. around t_5).

In (VIII) tumbling, the l_d domains remain anchored at the tips throughout the vesicle's rotation. The vesicle alternates between elongated shapes, tilted along the flow direction (with inclination angle $\theta \in (0, \pi/2)$), and flattened shapes, tilted against the flow ($\theta \in (-\pi/2, 0)$). When elongated (e.g. at t_3), the vesicle adopts a thin, prolate shape, where the l_o domains are located in relatively low-curvature regions. When flattened (e.g. at t_5), the vesicle deforms into a more oblate shape under shear flow, causing the curvature at the l_o locations to decrease further. This curvature reduction lowers the surface energy. Such cyclic shape evolution, driven by the interplay between shear forces and surface tension heterogeneity, accounts for the periodic surface energy variations observed in the tumbling regime.

We note that the phase diagram presented in this section is constructed using a symmetric initial distribution of the l_d phase (see figure 8*b*). Although the detailed dynamical trajectories may vary when different initial conditions are used, the qualitative dynamical regimes and their underlying physical mechanisms remain robust. Additional simulations starting from random initial conditions, provided in Appendix E, confirm that the vesicle consistently evolves towards dynamical states that are identifiable as the same regime classes reported here. These results demonstrate that the phase behaviour captured

https://doi.org/10.1017/jfm.2026.11276 Published online by Cambridge University Press

by our model is governed primarily by the interplay between membrane heterogeneity and shear flow, rather than strictly by the particular choice of initial phase distribution.

5. Conclusion

We have developed a comprehensive, thermodynamically consistent phase-field model that accurately captures the intricate interplay among vesicle dynamics, membrane heterogeneity and shear flow. The model successfully reproduces experimental observations of lateral phase separation and shear-induced morphological transitions. This underscores the accuracy, versatility and predictive capability of the model and numerical methods.

Systematic variation of the bending rigidity contrast κ_B and capillary number Ca reveals six dynamic regimes, including three previously unreported: (I), (II) and (IV). These regimes organize into two critical regions – the 'low-rigidity full-dynamics belt' and the 'low-capillary full-dynamics belt' – where all six dynamical regimes coexist. Within regime (V), we further identify three subregimes that reflect the rich ring structure of domain redistribution under shear. Beyond bending effects, we uncover surface tension heterogeneity as a previously unknown mechanism that suffices to induce (VII) and (VIII), revealing a new pathway for vesicle dynamics under shear. This unveils a distinct physical mechanism for tuning vesicle dynamics.

These findings offer a comprehensive understanding of the role of membrane heterogeneity in governing vesicle dynamics under shear flow, providing new insights and design principles for tuneable vesicle-based carriers.

Supplementary movies. Supplementary movies are available at https://doi.org/10.1017/jfm.2026.11276.

Funding. S.T. and Z.G. acknowledge support by the National Natural Science Foundation of China (grant no. 12371387). S.M. and J.L. acknowledge partial support by the National Science Foundation of the USA through grants NSF-DMS 2309547 (S.M.) and NSF-DMS 2309800 (J.L.).

Declaration of interests. The authors report no conflict of interest.

Appendix A. Diffuse domain method

We describe the diffuse domain method used to extend membrane dynamics from the sharp interface Γ to the rectangular domain Ω. This extension is achieved through a surface delta function $\zeta(\phi)$ (2.7), constructed from the phase-field variable ϕ, which is initialized with a hyperbolic tangent profile (2.1) to characterize the diffuse vesicle. The surface delta function $\zeta(\phi)$ satisfies the following approximation membrane (Teigen *et al.* 2011):

$$\int_{\Gamma} w \, \mathrm{d}S \approx \int_{\Omega} w\zeta(\phi) \, \mathrm{d}V, \tag{A1}$$

for any scalar or vector field w (e.g. c_Γ or $\boldsymbol{q}_c$). This relation enables the approximation of surface integrals and surface differential operators by volume integrals over Ω, facilitating the extension of surface quantities, equations and energy functionals into Ω.

We now describe the detailed procedure for coupling the surface phase separation dynamics, governed by the surface CH equation on Γ (2.10) to Ω. Using the diffuse domain method (Rätz & Voigt 2006; Li *et al.* 2009; Teigen *et al.* 2009), we assume that the membrane component c_Γ is smoothly extended off Γ, remaining constant in the normal direction within a narrow band around the membrane. This yields the normal extension

https://doi.org/10.1017/jfm.2026.11276 Published online by Cambridge University Press

condition:

$$\boldsymbol{n}(\boldsymbol{n}\cdot\nabla c_\Gamma)=\boldsymbol{0}. \tag{A2}$$

Additionally, since the diffusive flux $\boldsymbol{q}_c$ is tangential to Γ, its extension satisfies

$$\boldsymbol{n}\cdot\boldsymbol{q_c}=0. \tag{A3}$$

Using the incompressibility of the background fluid (2.3) and the surface gradient operator defined in (2.6), we derive the following identity near the vesicle membrane Γ:

$$\begin{aligned}\nabla_{\boldsymbol{\Gamma}}\cdot(c_\Gamma\boldsymbol{u}) &= (\nabla\cdot\boldsymbol{u}-\boldsymbol{n}\cdot\nabla\boldsymbol{u}\cdot\boldsymbol{n})\,c_\Gamma+\boldsymbol{u}\cdot(\nabla c_\Gamma-\boldsymbol{n}(\boldsymbol{n}\cdot\nabla c_\Gamma))\\ &= -(\boldsymbol{n}\cdot\nabla\boldsymbol{u}\cdot\boldsymbol{n})\,c_\Gamma+\boldsymbol{u}\cdot(\nabla c_\Gamma-\boldsymbol{n}(\boldsymbol{n}\cdot\nabla c_\Gamma))\,.\end{aligned} \tag{A4}$$

Applying the identity (A4) to the surface CH (2.10) yields

$$(c_\Gamma)_t-(\boldsymbol{n}\cdot(\nabla\boldsymbol{u})\cdot\boldsymbol{n})c_\Gamma+\boldsymbol{u}\cdot(\nabla c_\Gamma-\boldsymbol{n}(\boldsymbol{n}\cdot\nabla c_\Gamma))=\nabla\cdot\boldsymbol{q_c}-(\boldsymbol{n}\cdot\nabla)(\boldsymbol{n}\cdot\boldsymbol{q_c}). \tag{A5}$$

Moreover, we further employ the identity from James & Lowengrub (2004):

$$\partial_t\zeta(\phi)+\boldsymbol{u}\cdot\nabla\zeta(\phi)=-(\boldsymbol{n}\cdot\nabla\boldsymbol{u}\cdot\boldsymbol{n})\zeta(\phi). \tag{A6}$$

Multiplying (A5) by $\zeta(\phi)$, and (A6) by c_Γ, with the help of the assumptions (A2) and (A3), we obtain

$$(\zeta(\phi)c_\Gamma)_t+\nabla\cdot(\zeta(\phi)c_\Gamma\boldsymbol{u})=\zeta(\phi)\nabla\cdot\boldsymbol{q_c}. \tag{A7}$$

For the flux term, noting that $\zeta(\phi)$ varies predominantly in the normal direction near Γ with negligible tangential variation (especially for thin interfaces) and applying (A3), we obtain

$$\begin{aligned}\nabla\cdot(\zeta(\phi)\boldsymbol{q_c}) &= \zeta(\phi)\nabla\cdot\boldsymbol{q_c}+\nabla\zeta(\phi)\cdot\boldsymbol{q_c}\\ &= \zeta(\phi)\nabla\cdot\boldsymbol{q_c}+\nabla_{\boldsymbol{\Gamma}}\zeta(\phi)\cdot\boldsymbol{q_c}+(\boldsymbol{n}\cdot\nabla\zeta(\phi))(\boldsymbol{n}\cdot\boldsymbol{q_c})\\ &= \zeta(\phi)\nabla\cdot\boldsymbol{q_c}.\end{aligned} \tag{A8}$$

Thus, the resulting surface CH equation in diffuse domain formulation within Ω can be written as

$$(\zeta(\phi)c_\Gamma)_t+\nabla\cdot(\zeta(\phi)c_\Gamma\boldsymbol{u})=\nabla\cdot(\zeta(\phi)\boldsymbol{q_c})\,. \tag{A9}$$

Notably, previous studies have demonstrated that in the diffuse domain method, the extended PDE (A9) asymptotically converges to the original surface PDE (2.10) as the diffuse interface thickness approaches zero, $\varepsilon_\phi\to 0$ (Li *et al.* 2009; Yu *et al.* 2012; Lervåg & Lowengrub 2015; Chadwick *et al.* 2018; Poulsen & Voorhees 2018; Yu *et al.* 2020; Guo *et al.* 2021; Guo 2023).

Appendix B. Model derivation

Next, we derive the free energy dissipation law and the governing equations for the coupled multicomponent vesicle–fluid system. In accordance with the second law of thermodynamics, the free energy $\mathcal{F}$ (2.13) must satisfy the following dissipation law:

$$\frac{\mathrm{d}\mathcal{F}}{\mathrm{d}t}=\int_\Omega\frac{\delta\mathcal{F}}{\delta\boldsymbol{u}}\boldsymbol{u}_t+\frac{\delta\mathcal{F}}{\delta\phi}\phi_t+\frac{\delta\mathcal{F}}{\delta c_\Gamma}(c_\Gamma)_t\,\mathrm{d}V\le 0, \tag{B1}$$

where $\delta\mathcal{F}/\delta\boldsymbol{u}$, $\delta\mathcal{F}/\delta\phi$ and $\delta\mathcal{F}/\delta c_\Gamma$ denote the variational derivatives of the free energy $\mathcal{F}$ with respect to $\boldsymbol{u}$, ϕ and c_Γ, respectively.

For the fluid velocity field $\boldsymbol{u}$, the variational derivative of the free energy $\mathcal{F}$ (2.13) with respect to $\boldsymbol{u}$ is combined with the momentum conservation (2.2), applying integration by

https://doi.org/10.1017/jfm.2026.11276 Published online by Cambridge University Press

parts, we obtain

$$\int_\Omega \frac{\delta \mathcal{F}}{\delta \boldsymbol{u}} \boldsymbol{u}_t \,\mathrm{d}V = \int_\Omega \frac{\delta \mathcal{F}_K}{\delta \boldsymbol{u}} \boldsymbol{u}_t \,\mathrm{d}V = \int_\Omega \rho \boldsymbol{u} \cdot \boldsymbol{u}_t \,\mathrm{d}V$$
$$= \int_\Omega -\mu |\boldsymbol{D}(\boldsymbol{u})|^2 + \boldsymbol{F} \cdot \boldsymbol{u} - \xi \varepsilon_\phi^2 \phi^2 \, |\nabla \lambda_{local}|^2 \,\mathrm{d}V. \tag{B2}$$

Similarly, for the phase-field variable ϕ, the variational derivative of $\mathcal{F}$ with respect to ϕ yields

$$\begin{aligned}\frac{\delta \mathcal{F}}{\delta \phi} &= \frac{\delta \mathcal{F}_L}{\delta \phi} + \frac{\delta \mathcal{F}_S}{\delta \phi} + \frac{\delta \mathcal{F}_B}{\delta \phi} + \frac{\delta \mathcal{F}_A}{\delta \phi} \\ &= \left(\sigma_L \delta(c_\Gamma) + \sigma_S(c_\Gamma) + M_s \frac{S(\phi) - S(\phi_0)}{S(\phi_0)} \right) \omega_\phi \\ &\quad - \eta_\phi \varepsilon_\phi \nabla \left(\sigma_L \delta(c_\Gamma) + \sigma_S(c_\Gamma) + M_s \frac{S(\phi) - S(\phi_0)}{S(\phi_0)} \right) \cdot \nabla \phi \\ &\quad + \kappa_B(c_\Gamma) \eta_\phi \frac{f''(\phi)}{{\varepsilon_\phi}^2} \omega_\phi - \eta_\phi \Delta \left(\kappa_B(c_\Gamma) \omega_\phi \right), \end{aligned} \tag{B3}$$

where

$$\omega_\phi = \eta_\phi \left(\frac{f'(\phi)}{\varepsilon_\phi} - \varepsilon_\phi \Delta \phi \right). \tag{B4}$$

Combining (B3) with the CH evolution equation for the vesicle membrane (2.4) and applying integration by parts, we obtain

$$\begin{aligned}\int_\Omega \frac{\delta \mathcal{F}}{\delta \phi} \phi_t \,\mathrm{d}V = \int_\Omega & -\boldsymbol{q_\phi} \cdot \nabla \left[(b + \omega_c c_\Gamma) \, \omega_\phi - \eta_\phi \varepsilon_\phi \nabla \, (b + \omega_c c_\Gamma) \cdot \nabla \phi \right. \\ & \left. + \kappa_B(c_\Gamma) \eta_\phi \frac{f''(\phi)}{{\varepsilon_\phi}^2} \omega_\phi - \eta_\phi \Delta \left(\kappa_B(c_\Gamma) \omega_\phi \right) \right] \\ & - \boldsymbol{u} \cdot \nabla \phi \left[(b + \omega_c c_\Gamma) \, \omega_\phi - \eta_\phi \varepsilon_\phi \nabla \, (b + \omega_c c_\Gamma) \cdot \nabla \phi \right. \\ & \left. + \kappa_B(c_\Gamma) \eta_\phi \frac{f''(\phi)}{{\varepsilon_\phi}^2} \omega_\phi - \eta_\phi \Delta \left(\kappa_B(c_\Gamma) \omega_\phi \right) \right] \mathrm{d}V, \end{aligned} \tag{B5}$$

where

$$b = \sigma_L \delta(c_\Gamma) + \sigma_S(c_\Gamma) + M_s \frac{S(\phi) - S(\phi_0)}{S(\phi_0)} - \omega_c c_\Gamma. \tag{B6}$$

For the membrane component field c_Γ, multiplying both sides of (2.11) by the chemical potential ω_c, defined as the variational derivative of $\mathcal{F}$ with respect to c_Γ,

$$\begin{aligned}\zeta(\phi)\omega_c = \frac{\delta \mathcal{F}}{\delta c_\Gamma} &= \frac{\delta \mathcal{F}_L}{\delta c_\Gamma} + \frac{\delta \mathcal{F}_S}{\delta c_\Gamma} + \frac{\delta \mathcal{F}_B}{\delta c_\Gamma} \\ &= \frac{{\varepsilon_\phi}^{-1}}{2} {\kappa_B}'(c_\Gamma) {\omega_\phi}^2 + {\sigma_S}'(c_\Gamma) \zeta(\phi) + \sigma_L \zeta(\phi) \left(\eta_c \frac{f'(c_\Gamma)}{\varepsilon_c} - \eta_c \varepsilon_c \Delta c_\Gamma \right) \\ &\quad - \sigma_L \eta_c \varepsilon_c \nabla \zeta(\phi) \cdot \nabla c_\Gamma, \end{aligned} \tag{B7}$$

we obtain

$$\omega_c (\zeta(\phi) c_\Gamma)_t + \omega_c \nabla \cdot (\zeta(\phi) c_\Gamma \boldsymbol{u}) = \omega_c \nabla \cdot (\zeta(\phi) \boldsymbol{q_c}). \tag{B8}$$

https://doi.org/10.1017/jfm.2026.11276 Published online by Cambridge University Press

Using the definition of the chemical potential ω_c (B7), (2.4) and (2.11), which describe membrane evolution and the component dynamics of phase separation, respectively, we derive

$$\begin{aligned}\int_\Omega \frac{\delta \mathcal{F}}{\delta c_\Gamma}(c_\Gamma)_t \,\mathrm{d}V &= \int_\Omega \omega_c \nabla\cdot\boldsymbol{j} - \omega_c c_\Gamma(\zeta(\phi))_t \,\mathrm{d}V \\ &= \int_\Omega \omega_c \nabla\cdot\boldsymbol{j} - \phi_t\left(\omega_c c_\Gamma \omega_\phi - \eta_\phi \varepsilon_\phi \nabla\left(\omega_c c_\Gamma\right)\cdot\nabla\phi\right) \mathrm{d}V \\ &= \int_\Omega \phi_t\left(-\omega_c c_\Gamma \omega_\phi + \eta_\phi\varepsilon_\phi \nabla\left(\omega_c c_\Gamma\right)\cdot\nabla\phi\right) - \zeta(\phi)\nabla\omega_c\cdot\boldsymbol{q_c} \\ &\quad - \omega_c \nabla(\zeta(\phi)c_\Gamma)\cdot\boldsymbol{u}\,\mathrm{d}V \\ &= \int_\Omega -\boldsymbol{q_\phi}\cdot\nabla\left(-\omega_c c_\Gamma\omega_\phi + \eta_\phi\varepsilon_\phi\nabla\left(\omega_c c_\Gamma\right)\cdot\nabla\phi\right) - \zeta(\phi)\nabla\omega_c\cdot\boldsymbol{q_c} \\ &\quad - \boldsymbol{u}\cdot\left[\nabla\phi\left(-\omega_c c_\Gamma\omega_\phi + \eta_\phi\varepsilon_\phi\nabla\left(\omega_c c_\Gamma\right)\cdot\nabla\phi\right) + \omega_c\nabla(\zeta(\phi)c_\Gamma)\right]\mathrm{d}V,\end{aligned} \tag{B9}$$

where $\boldsymbol{j} = \zeta(\phi)\boldsymbol{q_c} - \zeta(\phi)c_\Gamma\boldsymbol{u}$.

Finally, by substituting (B2), (B5) and (B9) into the free energy dissipation law (B1), we obtain

$$\begin{aligned}\frac{\mathrm{d}\mathcal{F}}{\mathrm{d}t} &= \int_\Omega \frac{\delta\mathcal{F}}{\delta\boldsymbol{u}}\boldsymbol{u}_t + \frac{\delta\mathcal{F}}{\delta\phi}\phi_t + \frac{\delta\mathcal{F}}{\delta c_\Gamma}(c_\Gamma)_t\,\mathrm{d}V \\ &= \int_\Omega -\boldsymbol{q_\phi}\cdot\nabla\left[b\omega_\phi + \kappa_B(c_\Gamma)\eta_\phi\frac{f''(\phi)}{{\varepsilon_\phi}^2}\omega_\phi - \eta_\phi\Delta(\kappa_B(c_\Gamma)\omega_\phi) - \eta_\phi\varepsilon_\phi\nabla b\cdot\nabla\phi\right] \\ &\quad - \boldsymbol{u}\cdot\left[\nabla\phi\left[b\omega_\phi + \kappa_B(c_\Gamma)\eta_\phi\frac{f''(\phi)}{{\varepsilon_\phi}^2}\omega_\phi\right.\right. \\ &\quad \left.\left. - \eta_\phi\ \Delta(\kappa_B(c_\Gamma)\omega_\phi) - \eta_\phi\varepsilon_\phi\nabla b\cdot\nabla\phi + \omega_c\nabla(\zeta(\phi)c_\Gamma)\right]\right] \\ &\quad - \mu\,|\nabla\boldsymbol{u}|^2 + \boldsymbol{F}\cdot\boldsymbol{u} - \xi\varepsilon_\phi^2\phi^2\,|\nabla\lambda_{local}|^2 - \zeta(\phi)\nabla\omega_c\cdot\boldsymbol{q_c}\,\mathrm{d}V \le 0.\end{aligned} \tag{B10}$$

From these relations, we derive explicit expressions for the previously undetermined terms $\boldsymbol{F}$, $\boldsymbol{q}_\phi$ and $\boldsymbol{q}_c$ in (2.2)–(2.5) and (2.11),

$$\boldsymbol{F} = g\nabla\phi + \omega_c\nabla(\zeta(\phi)c_\Gamma), \tag{B11}$$

$$\boldsymbol{q_\phi} = m(\phi)\nabla g, \tag{B12}$$

$$\boldsymbol{q_c} = m(c_\Gamma)\nabla\omega_c, \tag{B13}$$

where

$$g = b\omega_\phi + \left(\kappa_B(c_\Gamma)\eta_\phi\frac{f''(\phi)}{{\varepsilon_\phi}^2}\omega_\phi - \eta_\phi\Delta(\kappa_B(c_\Gamma)\omega_\phi)\right) - \eta_\phi\varepsilon_\phi\nabla b\cdot\nabla\phi, \tag{B14}$$

$$b = -\omega_c c_\Gamma + \sigma_L\delta(c_\Gamma) + \mathrm{M}_s\frac{S(\phi) - S(\phi_0)}{S(\phi_0)} + Cs_\Gamma\sigma_S(c_\Gamma). \tag{B15}$$

Here, the functions $m(\phi) = D_\phi(1-\phi^2)^2$ and $m(c_\Gamma) = D_c(1-c_\Gamma^2)^2$ denote the mobilities, which are phenomenological parameters with D_ϕ and D_c being the diffusion coefficients.

https://doi.org/10.1017/jfm.2026.11276 Published online by Cambridge University Press

By substituting (B11)–(B15) into (B10), we obtain the following free energy dissipation identity:

$$\begin{aligned}\frac{\mathrm{d}\mathcal{F}}{\mathrm{d}t} &= \int_{\Omega} \frac{\delta \mathcal{F}}{\delta \boldsymbol{u}} \boldsymbol{u}_t + \frac{\delta \mathcal{F}}{\delta \phi} \phi_t + \frac{\delta \mathcal{F}}{\delta c_\Gamma} (c_\Gamma)_t \, \mathrm{d}V \\ &= \int_{\Omega} -\mu \, |\nabla \boldsymbol{u}|^2 - m(\phi) |\boldsymbol{q_\phi}|^2 - \zeta(\phi) m(c_\Gamma) |\nabla \omega_c|^2 - \xi \varepsilon_\phi^2 \phi^2 \, |\nabla \lambda_{local}|^2 \leq 0. \quad \text{(B16)}\end{aligned}$$

This expression confirms the thermodynamic consistency of the model, with free energy monotonically decreasing due to viscous dissipation, diffusive fluxes and membrane tension relaxation.

Appendix C. Numerical method

To solve the coupled system numerically, we discretize the time interval $I = [0, T]$ into uniform time steps $\Delta t = t_{n+1} - t_n$. Time-dependent variables at the nth and $(n+1)$th time steps are denoted as $(\cdot)^n$ and $(\cdot)^{n+1}$, respectively.

At each time step, the solution procedure consists of the following sequential steps.

(i) We first solve the CH (2.19) governing the membrane evolution to update ϕ^{n+1}, g^{n+1} and ω_ϕ^{n+1} by the following method:

$$\frac{\phi^{n+1} - \phi^n}{\Delta t} + \nabla \cdot (\phi^n \boldsymbol{u}^n) = \frac{1}{Pe} \nabla \cdot \boldsymbol{q_\phi}^{n+1}, \quad \text{(C1)}$$

$$\boldsymbol{q_\phi}^{n+1} = m(\phi^n) \nabla g^{n+1}, \quad \text{(C2)}$$

$$g^{n+1} = b^n \omega_\phi^{n+1} + \frac{1}{Ca} \left(\kappa_B(c_\Gamma^n) \eta_\phi \frac{f''(\phi^n)}{{\varepsilon_\phi}^2} \omega_\phi^{n+1} - \eta_\phi \Delta \left(\kappa_B(c_\Gamma^n) \omega_\phi^{n+1} \right) \right) - \eta_\phi \varepsilon_\phi \nabla b^n \cdot \nabla \phi^n, \quad \text{(C3)}$$

$$b^n = -\omega_c^n c_\Gamma^n + Cn_\Gamma \delta(c_\Gamma^n) + \mathcal{M}_s \frac{S(\phi^n) - S(\phi_0)}{S(\phi_0)} + Cs_\Gamma \sigma_S(c_\Gamma^n), \quad \text{(C4)}$$

$$\omega_\phi^{n+1} = \eta_\phi \left(\frac{f'(\phi^{n+1})}{\varepsilon_\phi} - \varepsilon_\phi \Delta \phi^{n+1} \right). \quad \text{(C5)}$$

The nonlinear terms, such as $f'(\phi^{n+1})$ and $f''(\phi^{n+1})$, are linearized via a first-order Taylor expansion, as described in Lowengrub *et al.* (2016).

(ii) Next, we solve the CH (2.21) governing the diffusion of membrane components to update c_Γ^{n+1} and ω_c^{n+1} by the following method:

$$\frac{\zeta(\phi^{n+1}) c_\Gamma^{n+1} - \zeta(\phi^n) c_\Gamma^n}{\Delta t} + \nabla \cdot (\zeta(\phi^n) c_\Gamma^n \boldsymbol{u}^n) = \frac{1}{Pe_\Gamma} \nabla \cdot \left(\zeta(\phi^{n+1}) \boldsymbol{q_c}^{n+1} \right), \quad \text{(C6)}$$

$$\boldsymbol{q_c}^{n+1} = m\left(c_\Gamma^n\right) \nabla \omega_c^{n+1}, \quad \text{(C7)}$$

$$\begin{aligned}\zeta(\phi^{n+1}) \omega_c^{n+1} = {} & \frac{1}{Ca} \frac{{\varepsilon_\phi}^{-1}}{2} {\kappa_B}'\left(c_\Gamma^n\right) \left(\omega_\phi^{n+1} \right)^2 + Cs_\Gamma {\sigma_S}'\left(c_\Gamma^n\right) \zeta\left(\phi^{n+1}\right) \\ & + Cn_\Gamma \zeta\left(\phi^{n+1}\right) \left(\eta_c \frac{f'\left(c_\Gamma^{n+1}\right)}{\varepsilon_c} - \eta_c \varepsilon_c \Delta c_\Gamma^{n+1} \right) \\ & - Cn_\Gamma \eta_c \varepsilon_c \nabla \zeta\left(\phi^{n+1}\right) \cdot \nabla c_\Gamma^n. \quad \text{(C8)}\end{aligned}$$

https://doi.org/10.1017/jfm.2026.11276 Published online by Cambridge University Press

Here, the nonlinear term $f'(c_\Gamma^{n+1})$ is likewise linearized using a first-order Taylor expansion.

(iii) Finally, we solve the Navier–Stokes equations (2.17)–(2.18) for the background fluid together with the local inextensibility constraint (2.20) using a projection method, which includes the following substeps.

Step 1. (Temporary velocity prediction) We first solve for the temporary velocity $\tilde{\boldsymbol{u}}^{n+1}$,

$$\rho\left(\frac{\tilde{\boldsymbol{u}}^{n+1}-\boldsymbol{u}^n}{\Delta t}\right)+\rho\nabla\cdot\left(\boldsymbol{u}^n\otimes\boldsymbol{u}^n\right)=\frac{1}{Re}\nabla\cdot\left(\mu\left(\phi^{n+1}\right)\boldsymbol{D}\left(\tilde{\boldsymbol{u}}^{n+1}\right)\right)-\nabla p^n \tag{C9}$$

$$+\frac{1}{Re}\boldsymbol{F}^n+\nabla\cdot\left(\zeta\left(\phi^{n+1}\right)\boldsymbol{P}^n\lambda_{local}^n\right), \tag{C10}$$

$$\boldsymbol{F}^n=g^{n+1}\nabla\phi^{n+1}+\omega_c^{n+1}\nabla\left(\zeta\left(\phi^{n+1}\right)c_\Gamma^{n+1}\right), \tag{C11}$$

where $\mu(\phi^{n+1})=(1+\phi^{n+1})\mu_{in}/2+(1-\phi^{n+1})\mu_{out}/2$. The fields ϕ^{n+1}, g^{n+1}, c_Γ^{n+1} and ω_c^{n+1} are obtained from (C1)–(C8).

Step 2. (Pressure correction) We then solve for the pressure and then update the velocity field. Having in mind of the incompressibility constraint,

$$\nabla\cdot\boldsymbol{u}^{n+1}=0, \tag{C12}$$

the velocity correction is given by

$$\boldsymbol{u}^{n+1}=\tilde{\boldsymbol{u}}^{n+1}-\frac{\Delta t}{\rho}\nabla\tilde{p}^{n+1}. \tag{C13}$$

By combining (C12) and (C13), the pressure $\tilde{p}^{n+1}$ is obtained by solving the following Poisson equation:

$$\nabla^2\tilde{p}^{n+1}=\frac{\rho}{\Delta t}\nabla\cdot\tilde{\boldsymbol{u}}^{n+1}. \tag{C14}$$

Step 3. (Velocity and pressure update) The velocity $\boldsymbol{u}^{n+1}$ and pressure p^{n+1} are then updated as

$$\boldsymbol{u}^{n+1}=\tilde{\boldsymbol{u}}^{n+1}-\frac{\Delta t}{\rho}\nabla\tilde{p}^{n+1}, \tag{C15}$$

$$p^{n+1}=p^n+\tilde{p}^{n+1}. \tag{C16}$$

Step 4. (Local inextensibility correction) Finally, the Lagrange multiplier λ_{local}^{n+1} is then updated by the following method:

$$\xi\varepsilon_\phi^2\nabla\cdot\left(\left(\phi^{n+1}\right)^2\nabla\lambda_{local}^{n+1}\right)+\zeta\left(\phi^{n+1}\right)\boldsymbol{P}^{n+1}:\nabla\boldsymbol{u}^n=0; \tag{C17}$$

where $\boldsymbol{P}^{n+1}=\boldsymbol{I}-(\nabla\phi^{n+1}/|\nabla\phi^{n+1}|)\otimes(\nabla\phi^{n+1}/|\nabla\phi^{n+1}|)$.

In addition, Dirichlet boundary conditions can imposed on $\tilde{\boldsymbol{u}}$, consistent with $\boldsymbol{u}$ in (2.8), while no-flux boundary conditions are applied to ϕ, $\boldsymbol{q}_\phi$, c_Γ and $\boldsymbol{q}_c$ as in (2.9)–(2.12).

Appendix D. Numerical convergence tests

This appendix presents two numerical convergence studies designed to validate the diffuse-interface formulation and the numerical method described in Appendix C.

https://doi.org/10.1017/jfm.2026.11276 Published online by Cambridge University Press

The first test examines surface diffusion on a stationary spherical vesicle and provides direct quantitative comparison with an analytical solution. The second test evaluates grid-refinement behaviour for fully coupled vesicle dynamics in shear flow. Together, these tests demonstrate that the proposed formulation accurately captures interfacial transport and vesicle hydrodynamics, and that the computational parameters adopted in the main text ensure both accuracy and efficiency.

D.1. *Surface-diffusion convergence on a stationary spherical vesicle*

To validate the diffuse-interface formulation, we examine the diffusion of a membrane component on a stationary spherical vesicle, following Guo *et al.* (2021). The governing equation is

$$(\zeta(\phi)c_\Gamma)_t = \frac{1}{Pe_\Gamma}\nabla\cdot(\zeta(\phi)\nabla c_\Gamma), \tag{D1}$$

which evaluates the diffuse-domain representation of the membrane and the numerical implementation of the surface diffusion operator.

Under the axisymmetric setting, the surface concentration depends only on the polar angle, i.e. $c_\Gamma = c_\Gamma(\beta, t)$, and is independent of the azimuthal angle. We consider a spherical vesicle of radius $r_0 = 1$. The initial distribution of the membrane component is prescribed as

$$c_\Gamma(\beta, 0) = \frac{1}{2}\big(1 - \cos\beta\big), \tag{D2}$$

where β denotes the polar angle measured from the negative Z-axis, so that $\cos\beta = -z/r_0$.

Since the vesicle is stationary (so that $\phi_t = 0$), (D1) reduces on the spherical surface to the standard axisymmetric surface-diffusion equation

$$\partial_t c_\Gamma(\beta, t) = \frac{1}{Pe_\Gamma r_0^2}\left(\frac{\partial^2 c_\Gamma}{\partial\beta^2} + \cot\beta\,\frac{\partial c_\Gamma}{\partial\beta}\right) \tag{D3}$$

for $\beta \in [0, \pi]$, subject to the initial condition (D2) and the natural symmetry conditions $\partial_\beta c_\Gamma(0, t) = \partial_\beta c_\Gamma(\pi, t) = 0$ at the poles. This yields the analytical solution

$$c_\Gamma(\beta, t) = \frac{1}{2}\left[1 - \exp\left(-\frac{2t}{Pe_\Gamma r_0^2}\right)\cos\beta\right]. \tag{D4}$$

To compare the numerical solution with the analytical solution (D4), we solve (D1) on the computational domain $\bar{\Omega} = [-1.5, 1.5]^3$. The stationary spherical interface is represented by the phase field

$$\phi(\boldsymbol{x}, 0) = \frac{1}{2}\tanh\left(\frac{r_0 - r(\boldsymbol{x})}{2\sqrt{2}\varepsilon_\phi}\right) + \frac{1}{2}, \quad r(\boldsymbol{x}) = \sqrt{x^2 + y^2 + z^2}, \quad \boldsymbol{x} = (x, y, z) \in \bar{\Omega}. \tag{D5}$$

Both ϕ and c_Γ are stored at cell centres in the finite-difference discretization, while the membrane interface is defined as the isosurface $\phi = 0.5$, which does not in general coincide with grid points. To evaluate c_Γ on the membrane, the interface geometry is first extracted using a marching–cubes procedure Teigen *et al.* (2011), and the values of c_Γ at the interface vertices are then obtained by trilinear interpolation from the surrounding cell-centred data. The resulting interpolated interface values are compared with the

https://doi.org/10.1017/jfm.2026.11276 Published online by Cambridge University Press

ε_ϕ	h	L_∞ error	Order
0.32	3/8	5.89×10^{-2}	—
0.16	3/16	2.01×10^{-2}	1.55
0.08	3/32	4.82×10^{-3}	2.06
0.04	3/64	1.20×10^{-3}	2.01
0.02	3/128	3.06×10^{-4}	1.97

Table 2. Convergence of numerical solutions towards the analytical interface component at $t = 1$ for surface diffusion on a stationary vesicle.

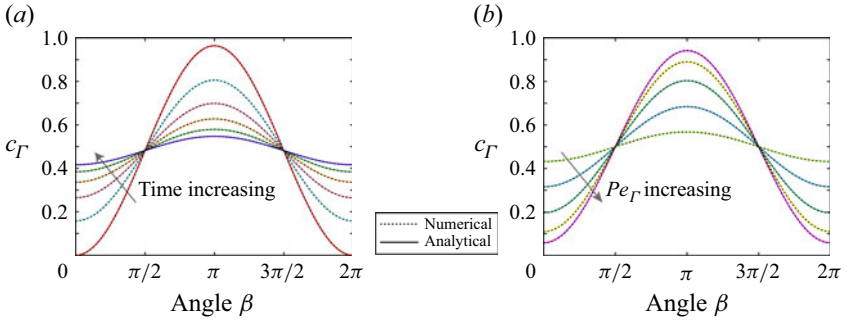


Figure 18. Comparison between numerical (dotted lines) and analytical (solid coloured lines) solutions for surface component diffusion on a stationary spherical vesicle. The grid spacing is $h = 3/128$ with $\varepsilon_\phi = 0.02$. (*a*) Temporal evolution at $Pe_\Gamma = 1$ for $t = 0,\ 0.2,\ 0.4,\ 0.6,\ 0.8,\ 1$. (*b*) Profiles at $t = 1$ for $Pe_\Gamma = 1,\ 2,\ 4,\ 8,\ 16$.

analytical solution at $t = 1$ to compute the L_∞ errors for various grid sizes and interface thicknesses ε_ϕ, as reported in table 2. For each refinement level, the time step Δt is reduced consistently with the mesh size so that temporal errors remain negligible compared with spatial discretization errors. Although the interpolation introduces a small auxiliary error, the results still exhibit clear second-order convergence with mesh refinement and decreasing interface thickness ε_ϕ.

For the profile comparisons shown in figure 18, c_Γ is additionally interpolated along a great circle cross-section on the plane $y = 0$, parametrized by the polar angle β. For visualization, the axisymmetric solution $c_\Gamma(\beta, t)$ is plotted over $\beta \in [0, 2\pi]$ by using its 2π-periodic extension. Figure 18(*a*) presents the temporal evolution of c_Γ at $Pe_\Gamma = 1$, demonstrating excellent agreement with the analytical solution. Figure 18(*b*) compares results at $t = 1$ for $Pe_\Gamma = 1, 2, 4, 8, 16$, confirming that the numerical method accurately captures the dependence on Pe_Γ. The corresponding diffusion patterns of c_Γ on the membrane for the temporal evolution in figure 18(*a*) are illustrated in figure 19.

D.2. *Convergence of the method and verification of domain parameters*

To further validate our numerical method, and to confirm that the computational domain parameters – in particular the grid resolution and time step size – are sufficient to accurately resolve the vesicle dynamics, we consider the evolution of a prepositioned multicomponent vesicle subjected to a shear flow of strength $\gamma = 1$. The computational domain is defined as $\bar{\Omega} = [-2, 2]^3$. The initial vesicle shape is prescribed using $d_1 = 1$

https://doi.org/10.1017/jfm.2026.11276 Published online by Cambridge University Press

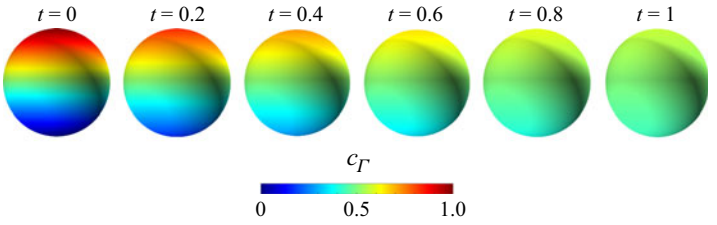


Figure 19. Diffusion patterns of the surface component c_Γ on the membrane corresponding to the temporal evolution shown in figure 18(*a*).

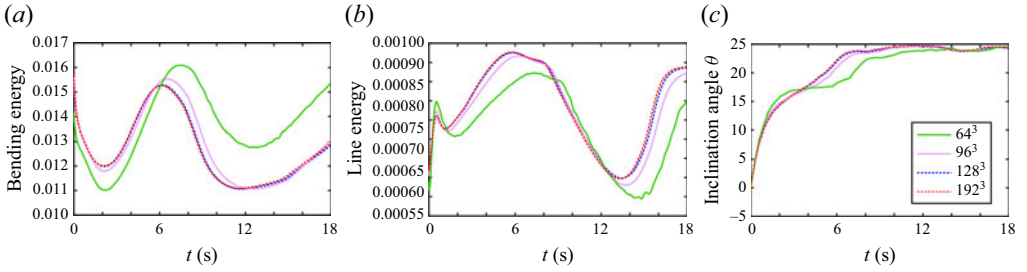


Figure 20. Grid-refinement study for an initially presegregated vesicle (figure 8*b*) in shear flow. Shown are the time evolutions of (*a*) bending energy, (*b*) line energy and (*c*) inclination angle for grids of size 64^3, 96^3, 128^3 and 192^3. The corresponding time step sizes are $\Delta t = 2 \times 10^{-4}$, 1.5×10^{-4}, 1×10^{-4} and 7.5×10^{-5}, respectively.

and $d_2 = d_3 = 0.565$, corresponding to a reduced volume of $v \approx 0.91$. The l_d phase is presegregated such that the area fraction is $a_{l_d} = 0.4$, as illustrated in figure 8(*b*).

To assess spatial convergence, simulations are performed on four uniform grids of size 64^3, 96^3, 128^3 and 192^3. For each grid, the time step sizes $\Delta t = 2 \times 10^{-4}$, 1.5×10^{-4}, 1×10^{-4}, 7.5×10^{-5}, respectively, are used. These choices maintain a comparable ratio between spatial and temporal resolutions, ensuring that differences observed in the results primarily reflect spatial accuracy. The dimensionless parameters used in all simulations are: $Re = 10^{-3}$, $Ca = 1$, $Cn_\Gamma = 0.05$, $Pe = 1000$, $Pe_\Gamma = 1$, $Cs_\Gamma = 10$, $\mathcal{M}_S = 2000$, $\sigma_S = 1$ and $k_B = 0.5$.

We monitor three quantities that characterize vesicle dynamics – namely (figure 20*a*) the bending energy, (figure 20*b*) the line energy, and (figure 20*c*) the inclination angle – and compare their evolution up to time $t = 18$. The simulations on the coarsest grid, 64^3, exhibit noticeable deviations from the finer-grid results across all three diagnostics, indicating insufficient spatial resolution. The 96^3 grid reduces but does not fully remove these discrepancies. In contrast, the 128^3 and 192^3 simulations produce nearly indistinguishable results for all three quantities, demonstrating convergence with respect to spatial refinement.

Since the 128^3 and 192^3 grids yield quantitatively and qualitatively identical vesicle dynamics, while the coarser grids (64^3 and 96^3) show clear under-resolution effects, we conclude that a grid of size 128^3 provides a reliable balance between computational accuracy and efficiency. Accordingly, a resolution of 128^3 is adopted for all simulations in this study.

https://doi.org/10.1017/jfm.2026.11276 Published online by Cambridge University Press

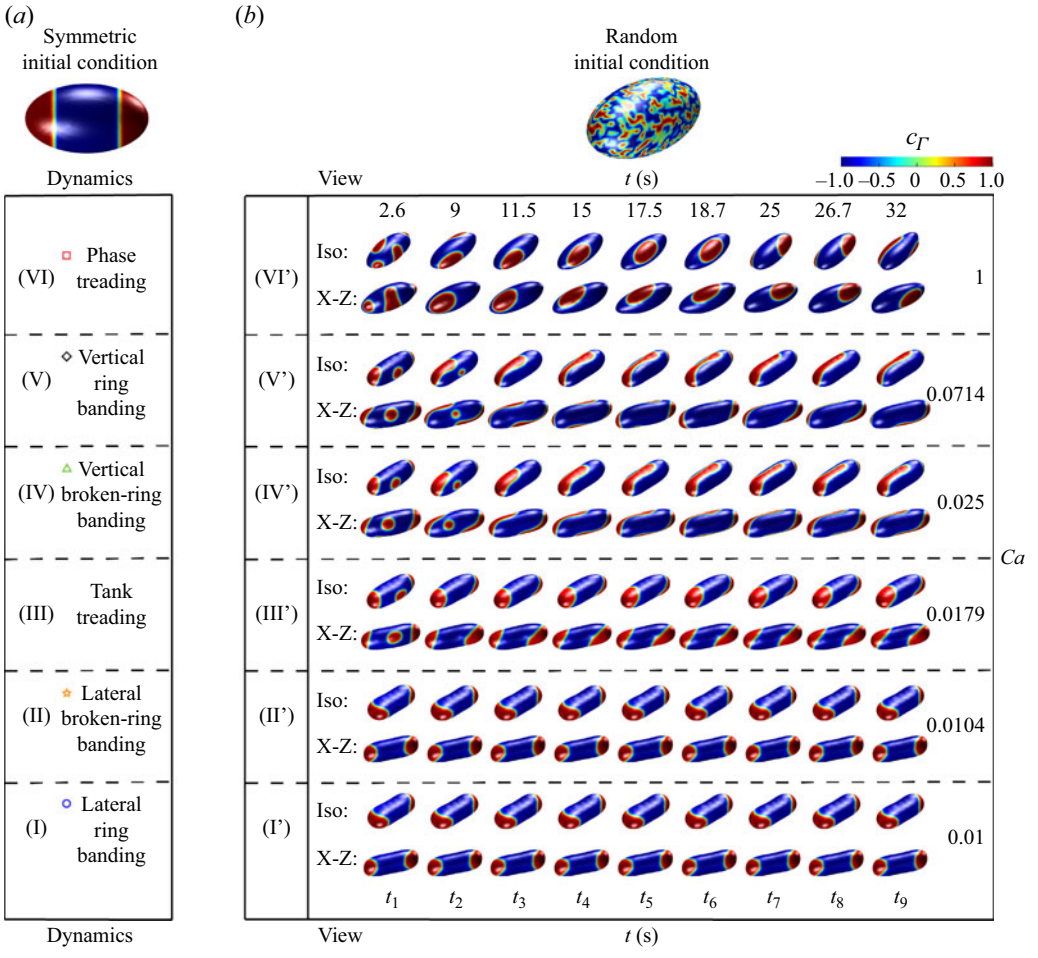


Figure 21. Comparison of vesicle dynamical regimes at $k_B = 0.65$ for varying Ca. (*a*) Dynamical regimes (I)–(VI) obtained from a symmetric initial condition (shown above the panel), corresponding to the classification presented in figure 14 of the original manuscript. (*b*) Time evolution of the corresponding regimes (I')–(VI') obtained under the same (k_B, Ca) values but starting from a random initial condition (also shown above the panel).

Appendix E. Dynamical regimes using random initial conditions

To examine the dependence of the dynamical regimes on the initial distribution of membrane components, we performed simulations starting from a random initial distribution of the l_d phase with the same area fraction $a_{l_d} = 0.4$, for several parameter combinations spanning regimes (I)–(VIII) in the phase diagrams, including those in figures 14(*a*) and 17(*a*). For each parameter set, we compare the time evolution obtained from the symmetric initial condition with that obtained from the random initial condition, using the same time instances as in the corresponding figures. The results for random initial conditions are shown in figures 21 and 22, where we denote the dynamical states by (I')–(VIII') to distinguish them from their symmetric counterparts.

For regimes (I)–(VI) in figure 14(*a*), the random initial condition generally leads to dynamical behaviours that are qualitatively similar – but not strictly identical – to those in the phase diagram. In particular, (III') and (IV') recover the same tank-treading and vertical broken-ring banding behaviours observed in (III) and (IV): both the vesicle shape

https://doi.org/10.1017/jfm.2026.11276 Published online by Cambridge University Press

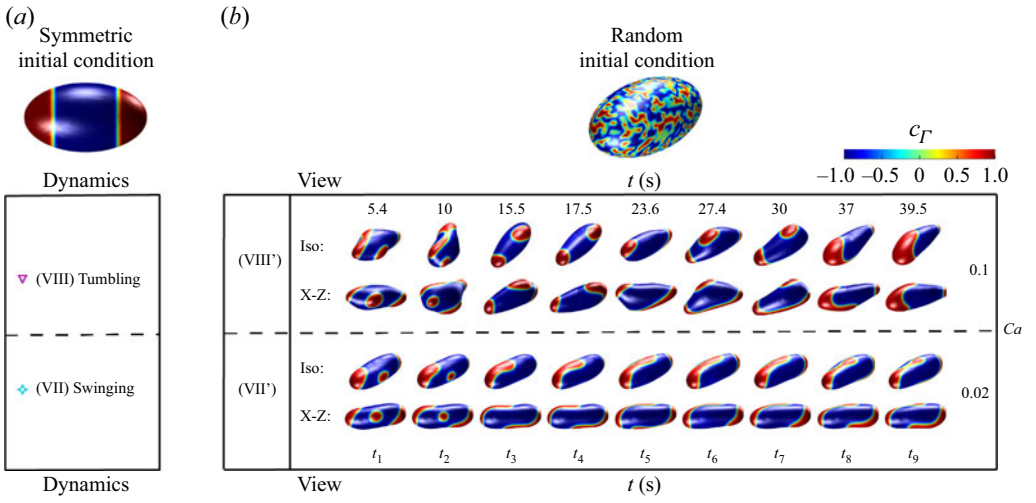


Figure 22. Comparison of vesicle dynamical regimes at $k_B = 0.65$ and $\sigma_S = 0.85$ for varying Ca. (a) Dynamical regimes (VII)–(VIII) obtained from a symmetric initial condition (shown above the panel), corresponding to the classification presented in figure 17(a). (b) Time evolution of the corresponding regimes (VII')–(VIII') obtained under the same (σ_S, Ca) values but starting from a random initial condition (also shown above the panel).

and the organization of the l_d domains are very close to those obtained from the symmetric initial condition. By contrast, (I'), (II'), (V') and (VI') exhibit behaviours that remain clearly related to (I), (II), (V) and (VI), but with noticeable differences.

For (I') and (II'), the vesicle no longer adopts a strongly oblate shape, yet the softer l_d phase still migrates robustly towards the tips and accumulates there. We attribute this to the random initial distribution: because the l_d phase is initially scattered over the membrane, the domains can reorganize and migrate towards the tips while the vesicle shape adjusts more gradually, without necessarily passing through a strongly oblate configuration to minimize bending energy.

For (V') and (VI'), the stronger shear accelerates phase separation from the random initial condition, but the l_d domains do not evolve into two perfectly symmetric caps as in (V) and (VI). As a result, the dynamics do not form an ideal single, slender vertical band (V'), nor a strictly periodic phase-treading motion between two symmetric tips (VI'). Nevertheless, the essential features persist: in (V'), the two l_d-rich regions still migrate towards the tips and elongate along the flow direction, although they do not merge into a continuous vertical ring; in (VI'), the l_d phase still travels back and forth between the two tip regions, but with more irregularity due to the asymmetry introduced by the random initial distribution.

For regimes (VII)–(VIII) in figure 17(a), which probe the effect of composition-dependent surface tension under shear, the simulations with random initial conditions likewise exhibit the same categories of dynamical responses. In (VII'), we again observe swinging-like behaviour, though with less regular oscillations due to the asymmetric initial l_d distribution. In (VIII'), the vesicle displays a tumbling-like motion, but the l_d phase separates into multiple distinct patches. The lower surface tension in the l_d regions allows local outward protrusions, creating shape asymmetries that, together with shear, yield a more irregular tumbling cycle. For the particular parameter shown in figure 22(b) (VIII'), the relatively strong shear amplifies the influence of the asymmetric domain pattern. However, within the same parameter region as (VIII) in figure 16(a), we also tested cases

https://doi.org/10.1017/jfm.2026.11276 Published online by Cambridge University Press

with slightly weaker shear, for which more regular tumbling dynamics are recovered even under random initial conditions.

Taken together, these additional simulations demonstrate that the phase diagram in § 4 is not strictly independent of the initial condition, in the sense that different initial distributions may lead to differences in domain rearrangements or symmetry at the same parameter point. However, the qualitative dynamical regimes and the underlying physical mechanisms are robust: starting from a random initial condition primarily affects the detailed morphology of the domains, while the vesicle still evolves towards dynamical states that are clearly recognizable as the same classes reported in the phase diagram (figures 13*a* and 16*a*). In particular, the key signatures of the interplay among membrane heterogeneity, shear flow and phase separation – such as preferential accumulation of the softer phase in high-curvature regions and shear-induced reorganization of domains – remain unchanged.

References

Abkarian, M. & Viallat, A. 2005 Dynamics of vesicles in a wall-bounded shear flow. *Biophys. J.* **89** (2), 1055–1066.

Aland, S., Egerer, S., Lowengrub, J. & Voigt, A. 2014 Diffuse interface models of locally inextensible vesicles in a viscous fluid. *J. Comput. Phys.* **277**, 32–47.

Allen, T.M. & Cullis, P.R. 2004 Drug delivery systems: entering the mainstream. *Science* **303** (5665), 1818–1822.

Anderson, V.J. & Lekkerkerker, H.N.W. 2002 Insights into phase transition kinetics from colloid science. *Nature* **416** (6883), 811–815.

Arroyo, M. & DeSimone, A. 2009 Relaxation dynamics of fluid membranes. *Phys. Rev. E* **79** (3), 031915.

Baumgart, T., Das, S., Webb, W.W. & Jenkins, J.T. 2005 Membrane elasticity in giant vesicles with fluid phase coexistence. *Biophys. J.* **89** (2), 1067–1080.

Baumgart, T., Hess, S.T. & Webb, W.W. 2003 Imaging coexisting fluid domains in biomembrane models coupling curvature and line tension. *Nature* **425** (6960), 821–824.

Chadwick, A.F., Stewart, J.A., Enrique, R.A., Du, S. & Thornton, K. 2018 Numerical modeling of localized corrosion using phase-field and smoothed boundary methods. *J. Electrochem. Soc.* **165** (10), C633–C646.

Colom, A., Derivery, E., Soleimanpour, S., Tomba, C., Molin, M.D., Sakai, N., González-Gaitán, M., Matile, S. & Roux, A. 2018 A fluorescent membrane tension probe. *Nat. Chem.* **10** (11), 1118–1125.

Danker, G., Biben, T., Podgorski, T., Verdier, C. & Misbah, C. 2007 Dynamics and rheology of a dilute suspension of vesicles: higher order theory. *Phys. Rev. E* **76** (4), 041905.

Deschamps, J., Kantsler, V. & Steinberg, V. 2009 Phase diagram of single vesicle dynamical states in shear flow. *Phys. Rev. Lett.* **102** (11), 118105.

Destainville, N., Manghi, M. & Cornet, J. 2018 A rationale for mesoscopic domain formation in biomembranes. *Biomolecules* **8** (4), 104.

Elani, Y., Law, R.V. & Ces, O. 2014 Vesicle-based artificial cells as chemical microreactors with spatially segregated reaction pathways. *Nat. Commun.* **5** (1), 5305.

Evans, E. & Rawicz, W. 1990 Entropy-driven tension and bending elasticity in condensed-fluid membranes. *Phys. Rev. Lett.* **64** (17), 2094–2097.

Gera, P. & Salac, D. 2018*a* Modeling of multicomponent three-dimensional vesicles. *Comput. Fluids* **172**, 362–383.

Gera, P. & Salac, D. 2018*b* Three-dimensional multicomponent vesicles: dynamics and influence of material properties. *Soft Matt.* **14** (37), 7690–7705.

Gera, P., Salac, D. & Spagnolie, S.E. 2022 Swinging and tumbling of multicomponent vesicles in flow. *J. Fluid Mech.* **935**, A39.

Guo, Z. 2023 Nonlinear coupling effects of the thermocapillarity and insoluble surfactants to droplet migration under Poiseuille flow. *Phys. Rev. Fluids* **8** (2), 024001.

Guo, Z., Lin, P., Lowengrub, J. & Wise, S.M. 2017 Mass conservative and energy stable finite difference methods for the quasi-incompressible Navier–Stokes–Cahn–Hilliard system: primitive variable and projection-type schemes. *Comput. Meth. Appl. Mech. Engng* **326**, 144–174.

https://doi.org/10.1017/jfm.2026.11276 Published online by Cambridge University Press

GUO, Z., YU, F., LIN, P., WISE, S. & LOWENGRUB, J. 2021 A diffuse domain method for two-phase flows with large density ratio in complex geometries. *J. Fluid Mech.* **907**, A38.
HERRMANN, I.K., WOOD, M.J.A. & FUHRMANN, G. 2021 Extracellular vesicles as a next-generation drug delivery platform. *Nat. Nanotechnology* **16** (7), 748–759.
JAMES, A.J. & LOWENGRUB, J. 2004 A surfactant-conserving volume-of-fluid method for interfacial flows with insoluble surfactant. *J. Comput. Phys.* **201** (2), 685–722.
KANTSLER, V. & STEINBERG, V. 2006 Transition to tumbling and two regimes of tumbling motion of a vesicle in shear flow. *Phys. Rev. Lett.* **96** (3), 036001.
KARAZ, S. & SENSES, E. 2023 Liposomes under shear: structure, dynamics, and drug delivery applications. *Adv. NanoBiomed Res.* **3** (4), 2200101.
KELLER, S.R. & SKALAK, R. 1982 Motion of a tank-treading ellipsoidal particle in a shear flow. *J. Fluid Mech.* **120**, 27–47.
KOOIJMANS, S.A.A., DE JONG, O.G. & SCHIFFELERS, R.M. 2021 Exploring interactions between extracellular vesicles and cells for innovative drug delivery system design. *Adv. Drug Deliv. Rev.* **173**, 252–278.
LEBEDEV, V.V., TURITSYN, K.S. & VERGELES, S.S. 2008 Nearly spherical vesicles in an external flow. *New J. Phys.* **10** (4), 043044.
LERVÅG, K.Y. & LOWENGRUB, J. 2015 Analysis of the diffuse-domain method for solving PDEs in complex geometries. *Commun. Math. Sci.* **13** (6), 1473–1500.
LI, S., LOWENGRUB, J. & VOIGT, A. 2012 Locomotion, wrinkling, and budding of a multicomponent vesicle in viscous fluids. *Commun. Math. Sci.* **10** (2), 645–670.
LI, X., LOWENGRUB, J., RÄTZ, A. & VOIGT, A. 2009 Solving pdes in complex geometries: a diffuse domain approach. *Commun. Math. Sci.* **7** (1), 81.
LINDBLOM, G. & ORÄDD, G. 1994 NMR studies of translational diffusion in lyotropic liquid crystals and lipid membranes. *Prog. Nucl. Magn. Res. Spectrosc.* **26**, 483–515.
LINGWOOD, D. & SIMONS, K. 2010 Lipid rafts as a membrane-organizing principle. *Science* **327** (5961), 46–50.
LIU, K., MARPLE, G.R., ALLARD, J., LI, S., VEERAPANENI, S. & LOWENGRUB, J. 2017 Dynamics of a multicomponent vesicle in shear flow. *Soft Matt.* **13** (19), 3521–3531.
LOWENGRUB, J., ALLARD, J. & ALAND, S. 2016 Numerical simulation of endocytosis: viscous flow driven by membranes with non-uniformly distributed curvature-inducing molecules. *J. Comput. Phys.* **309**, 112–128.
LOWENGRUB, J.S., XU, J.J. & VOIGT, A. 2007 Surface phase separation and flow in a simple model of multicomponent drops and vesicles. *Fluid Dyn. Mater. Process.* **3** (1), 1–20.
LUBY-PHELPS, K. 1999*a* International Review of Cytology. *Intl Rev. Cytology* **192**, 189–221.
LUBY-PHELPS, K. 1999*b* Cytoarchitecture and physical properties of cytoplasm: volume, viscosity, diffusion, intracellular surface area. *Intl Rev. Cytology* **192**, 189–221.
MISBAH, C. 2006 Vacillating breathing and tumbling of vesicles under shear flow. *Phys. Rev. Lett.* **96** (2), 028104.
MUKHERJEE, S. & MAXFIELD, F.R. 2004 Membrane domains. *Annu. Rev. Biophys. Biomol. Struct.* **20** (1), 839–866.
NOGUCHI, H. & GOMPPER, G. 2007 Swinging and tumbling of fluid vesicles in shear flow. *Phys. Rev. Lett.* **98** (12), 128103.
POULSEN, S.O. & VOORHEES, P.W. 2018 Smoothed boundary method for diffusion-related partial differential equations in complex geometries. *Intl J. Comput. Meth.* **15** (03), 1850014.
REGAN, D., WILLIAMS, J., BORRI, P. & LANGBEIN, W. 2019 Lipid bilayer thickness measured by quantitative DIC reveals phase transitions and effects of substrate hydrophilicity. *Langmuir* **35** (43), 13805–13814.
RISSELADA, H.J. & MARRINK, S.J. 2008 The molecular face of lipid rafts in model membranes. *Proc. Natl Acad. Sci.* **105** (45), 17367–17372.
RÄTZ, A. & VOIGT, A. 2006 PDE's on surfaces — a diffuse interface approach. *Commun. Math. Sci.* **4** (3), 575–590.
SACKMANN, E. & SMITH, A.-S. 2014 Physics of cell adhesion: some lessons from cell-mimetic systems. *Soft Matt.* **10** (11), 1644.
SIMONS, K. & IKONEN, E. 1997 Functional rafts in cell membranes. *Nature* **387** (6633), 569–572.
SIMONS, K. & TOOMRE, D. 2000 Lipid rafts and signal transduction. *Nat. Rev. Mol. Cell Biol.* **1** (1), 31–39.
SIMONS, K. & VAZ, W.L.C. 2004 Model systems, lipid rafts, and cell membranes. *Annu. Rev. Biophys. Biomol. Struct.* **33** (1), 269–295.
SISCHKA, J.M. & VOIGT, A. 2025 Two-phase fluid deformable surfaces with constant enclosed volume and phase-dependent bending and Gaussian rigidity. *Comput. Meth. Appl. Mech. Engng* **445**, 118166.

https://doi.org/10.1017/jfm.2026.11276 Published online by Cambridge University Press

SOHN, J., LI, S., LI, X. & LOWENGRUB, J.S. 2012 Axisymmetric multicomponent vesicles: a comparison of hydrodynamic and geometric models. *Numer. Meth. Biomed. Engng* **28** (3), 346–368.

SOHN, J.S., TSENG, Y.-H., LI, S., VOIGT, A. & LOWENGRUB, J.S. 2010 Dynamics of multicomponent vesicles in a viscous fluid. *J. Comput. Phys.* **229** (1), 119–144.

TEIGEN, K.E., LI, X., LOWENGRUB, J., WANG, F. & VOIGT, A. 2009 A diffuse-interface approach for modeling transport, diffusion and adsorption/desorption of material quantities on a deformable interface. *Commun. Math. Sci.* **4** (7), 1009.

TEIGEN, K.E., SONG, P., LOWENGRUB, J. & VOIGT, A. 2011 A diffuse-interface method for two-phase flows with soluble surfactants. *J. Comput. Phys.* **230** (2), 375–393.

TIAN, A., JOHNSON, C., WANG, W. & BAUMGART, T. 2007 Line tension at fluid membrane domain boundaries measured by micropipette aspiration. *Phys. Rev. Lett.* **98** (20), 208102.

TUSCH, S., LOISEAU, E., AL-HALIFA, A.-H., KHELLOUFI, K., HELFER, E. & VIALLAT, A. 2018 When giant vesicles mimic red blood cell dynamics: swinging of two-phase vesicles in shear flow. *Phys. Rev. Fluids* **3** (12), 123605.

VAN SANTEN, R.A. 1984 The Ostwald step rule. *J. Phys. Chem.* **88** (24), 5768–5769.

VEATCH, S.L. & KELLER, S.L. 2003 Separation of liquid phases in giant vesicles of ternary mixtures of phospholipids and cholesterol. *Biophys. J.* **85** (5), 3074–3083.

VEATCH, S.L. & KELLER, S.L. 2005 Miscibility phase diagrams of giant vesicles containing sphingomyelin. *Phys. Rev. Lett.* **94** (14), 148101.

VEERAPANENI, S.K., YOUNG, Y.-N., VLAHOVSKA, P.M. & BŁAWZDZIEWICZ, J. 2011 Dynamics of a compound vesicle in shear flow. *Phys. Rev. Lett.* **106** (15), 158103.

VENKATESH, A. & NARSIMHAN, V. 2024 Shape dynamics of nearly spherical, multicomponent vesicles under shear flow. *J. Fluid. Mech.* **1020**, A49.

VLAHOVSKA, P.M. & GRACIA, R.S. 2007 Dynamics of a viscous vesicle in linear flows. *Phys. Rev. E* **75** (1), 016313.

WANG, Y., PALZHANOV, Y., QUAINI, A., OLSHANSKII, M. & MAJD, S. 2022 Lipid domain coarsening and fluidity in multicomponent lipid vesicles: a continuum based model and its experimental validation. *Biochim. Biophys. Acta (BBA) – Biomembranes* **1864** (7), 183898.

WIRTZ, D. 2009 Particle-tracking microrheology of living cells: principles and applications. *Annu. Rev. Biophys.* **38** (1), 301–326.

WU, H. & OU-YANG, Z.-C. 2025 A generalized helfrich free energy framework for multicomponent fluid membranes. *Membranes* **15** (6), 182.

YANAGISAWA, M., IMAI, M. & TANIGUCHI, T. 2008 Shape deformation of ternary vesicles coupled with phase separation. *Phys. Rev. Lett.* **100** (14), 148102.

YOUNG, Y.-N., VEERAPANENI, S. & MIKSIS, M.J. 2014 Long-wave dynamics of an inextensible planar membrane in an electric field. *J. Fluid Mech.* **751**, 406–431.

YU, F., GUO, Z. & LOWENGRUB, J. 2020 Higher-order accurate diffuse-domain methods for partial differential equations with dirichlet boundary conditions in complex, evolving geometries. *J. Comput. Phys.* **406**, 109174.

YU, H.-C., CHEN, H.-Y. & THORNTON, K. 2012 Extended smoothed boundary method for solving partial differential equations with general boundary conditions on complex boundaries. *Model. Simul. Mater. Sci. Engng* **20** (7), 075008.

ZHILIAKOV, A., WANG, Y., QUAINI, A., OLSHANSKII, M. & MAJD, S. 2021 Experimental validation of a phase-field model to predict coarsening dynamics of lipid domains in multicomponent membranes. *Biochim. Biophys. Acta* **1863** (1), 183446.

https://doi.org/10.1017/jfm.2026.11276 Published online by Cambridge University Press